

ARMY RESEARCH LABORATORY



**Dissipative Particle Dynamics at Isoenthalpic Conditions
Using Shardlow-Like Splitting Algorithms**

by John K. Brennan and Martin Lísal

ARL-TR-6587

September 2013

NOTICES

Disclaimers

The findings in this report are not to be construed as an official Department of the Army position unless so designated by other authorized documents.

Citation of manufacturer's or trade names does not constitute an official endorsement or approval of the use thereof.

Destroy this report when it is no longer needed. Do not return it to the originator.

Army Research Laboratory

Aberdeen Proving Ground, MD 21005-5066

ARL-TR-6587

September 2013

Dissipative Particle Dynamics at Isoenthalpic Conditions Using Shardlow-Like Splitting Algorithms

John K. Brennan

Weapons and Materials Research Directorate, ARL

Martin Lísal

**Institute of Chemical Process Fundamentals of the ASCR and
J. E. Purkinje University**

REPORT DOCUMENTATION PAGE			Form Approved OMB No. 0704-0188		
Public reporting burden for this collection of information is estimated to average 1 hour per response, including the time for reviewing instructions, searching existing data sources, gathering and maintaining the data needed, and completing and reviewing the collection information. Send comments regarding this burden estimate or any other aspect of this collection of information, including suggestions for reducing the burden, to Department of Defense, Washington Headquarters Services, Directorate for Information Operations and Reports (0704-0188), 1215 Jefferson Davis Highway, Suite 1204, Arlington, VA 22202-4302. Respondents should be aware that notwithstanding any other provision of law, no person shall be subject to any penalty for failing to comply with a collection of information if it does not display a currently valid OMB control number. PLEASE DO NOT RETURN YOUR FORM TO THE ABOVE ADDRESS.					
1. REPORT DATE (DD-MM-YYYY) September 2013		2. REPORT TYPE Final		3. DATES COVERED (From - To) February 2012–April 2013	
4. TITLE AND SUBTITLE Dissipative Particle Dynamics at Isoenthalpic Conditions Using Shardlow-Like Splitting Algorithms			5a. CONTRACT NUMBER		
			5b. GRANT NUMBER		
			5c. PROGRAM ELEMENT NUMBER		
6. AUTHOR(S) John K. Brennan and Martin Lísal*			5d. PROJECT NUMBER		
			5e. TASK NUMBER		
			5f. WORK UNIT NUMBER		
7. PERFORMING ORGANIZATION NAME(S) AND ADDRESS(ES) U.S. Army Research Laboratory ATTN: RDRL-WML-B Aberdeen Proving Ground, MD 21005-5066			8. PERFORMING ORGANIZATION REPORT NUMBER ARL-TR-6587		
9. SPONSORING/MONITORING AGENCY NAME(S) AND ADDRESS(ES)			10. SPONSOR/MONITOR'S ACRONYM(S)		
			11. SPONSOR/MONITOR'S REPORT NUMBER(S)		
12. DISTRIBUTION/AVAILABILITY STATEMENT Approved for public release; distribution is unlimited.					
13. SUPPLEMENTARY NOTES * Institute of Chemical Process Fundamentals of the ASCR and J. E. Purkinje University					
14. ABSTRACT A numerical integration scheme based upon the Shardlow-splitting algorithm (SSA) is presented for a Dissipative Particle Dynamics (DPD) approach at fixed pressure and enthalpy. A constant-enthalpy DPD method (DPD-H) is developed by combining the equations of motion (EOM) for a barostat with the EOM for the constant-energy DPD method (DPD-E). The DPD-H variant is developed for both a deterministic (Hoover) and stochastic (Langevin) barostat, where a <i>barostat temperature</i> is defined to satisfy the fluctuation-dissipation theorem for the Langevin barostat. The application of the Shardlow-splitting algorithm is particularly critical for the DPD-H variant because it allows more temporally practical simulations to be carried out. The DPD-H variant using the SSA is verified using both a standard DPD fluid model and a coarse-grain solid model. For both models, the DPD-H variant is further verified by instantaneously heating a slab of particles in the simulation cell and subsequently monitoring the evolution of the corresponding thermodynamic variables as the system approaches an equilibrated state while maintaining constant-enthalpy conditions. The Fokker-Planck equation and derivation of the fluctuation-dissipation theorem are included.					
15. SUBJECT TERMS dissipative particle dynamics, modeling, simulation, Shardlow-splitting algorithm, constant enthalpy					
16. SECURITY CLASSIFICATION OF:			17. LIMITATION OF ABSTRACT UU	18. NUMBER OF PAGES 50	19a. NAME OF RESPONSIBLE PERSON John K. Brennan
a. REPORT Unclassified	b. ABSTRACT Unclassified	c. THIS PAGE Unclassified			19b. TELEPHONE NUMBER (Include area code) 410-306-0678

Contents

List of Figures	iv
List of Tables	v
Acknowledgments	vi
1. Introduction	1
2. Formulations of DPD at Fixed Pressure and Enthalpy Using Shardlow-Like Splitting Numerical Discretization	2
2.1 General Formulation of DPD	2
2.2 Constant-Enthalpy DPD	3
3. Computational Details	9
4. Results	10
4.1 Test Case No. 1: Equivalence of DPD Variants.....	10
4.1.1 DPD Fluid.....	10
4.1.2 Coarse-Grain Solid.....	15
4.2 Test Case No. 2: Heating Response in DPD-H Simulations.....	16
4.2.1 DPD Fluid.....	16
4.2.2 Coarse-Grain Solid.....	21
4.3 Conservation of Total System Enthalpy.....	23
5. Conclusion	25
6. References	26
Appendix A. Fokker-Planck Equation (FPE) and Fluctuation-Dissipation Theorem (FDT)	29
Appendix B. Constant-Enthalpy Conditions (DPD-H) for Nonuniform Dilation	35
Appendix C. Simulation Model Details	39
List of Symbols, Abbreviations, and Acronyms	41
Distribution List	42

List of Figures

Figure 1. The probability distributions of (a) p_i , (b) u_i , and (c) V for DPD-H with a Langevin barostat. Symbols represent simulation results for $\Delta t = 0.01$, and lines correspond to (a) the Maxwell-Boltzmann distribution for p_i and (b, c) “exact” results, i.e., simulation results where $\Delta t = 0.001$	14
Figure 2. Time evolution of the kinetic temperature T_{kin} , internal temperature T_{int} , virial pressure P_{vir} , and particle density ρ for a DPD-H simulation of the pure DPD fluid at $P_0 = 23.65$, where a slab of particles in the simulation box was instantaneously heated by $T_{heat} = 10$ at $t = 0$: (a) DPD-H simulations using the Langevin barostat with a barostat temperature $T_{bar} = 1.0$, and (b) DPD-H simulations with a Hoover barostat. Insets display early time behavior of T_{kin} , T_{int} , ρ , and P_{vir}	18
Figure 3. Time evolution of the kinetic temperature T_{kin} , internal temperature T_{int} , and mass density ρ for a DPD-H simulation using a Langevin barostat with a barostat temperature $T_{bar} = 1300$ K for the coarse-grain solid at $P_0 = 0$ bar, where a slab of particles in the simulation box was instantaneously heated by $T_{heat} = 3000$ K at $t = 0$	22
Figure 4. The relative drift in H' as a function of the integration time step Δt for DPD-H simulations with the SSA-VV.....	24
Figure A-1. The probability distributions of (a) p_i , (b) u_i , and (c) V for DPD-H with a Langevin barostat. Symbols represent simulation results for $\Delta t = 0.01$, and lines correspond to (a) the Maxwell-Boltzmann distribution for p_i and (b, c) “exact” results, i.e., simulation results where $\Delta t = 0.001$	33

List of Tables

Table 1. The configurational energy per particle $\langle u \rangle$, the kinetic temperature $\langle T_{kin} \rangle$, the internal temperature $\langle T_{int} \rangle$, the virial pressure $\langle P_{vir} \rangle$, the particle density $\langle \rho \rangle$, and the self-diffusion coefficient D , determined from test case no. 1 simulations of the pure DPD fluid. T_{bar} is the Langevin barostat temperature and $\langle \cdot \rangle$ denotes an ensemble average, where numbers in parentheses are uncertainties calculated from block averages.	11
Table 2. The configurational energy per particle $\langle u \rangle$, the kinetic temperature $\langle T_{kin} \rangle$, the internal temperature $\langle T_{int} \rangle$, the virial pressure $\langle P_{vir} \rangle$, the particle density $\langle \rho \rangle$, and the self-diffusion coefficient D , determined from test case no. 1 simulations of the equimolar binary DPD fluid. T_{bar} is the Langevin barostat temperature and $\langle \cdot \rangle$ denotes an ensemble average, where numbers in parentheses are uncertainties calculated from block averages.	12
Table 3. The molar configurational energy $\langle u \rangle$, the kinetic temperature $\langle T_{kin} \rangle$, the internal temperature $\langle T_{int} \rangle$, the virial pressure $\langle P_{vir} \rangle$, and the mass density $\langle \rho \rangle$ determined from test case no. 1 simulations of the coarse-grain solid model of nickel. T_{bar} is the Langevin barostat temperature and $\langle \cdot \rangle$ denotes an ensemble average, where numbers in parentheses are uncertainties calculated from block averages.	15
Table 4. The kinetic temperature $\langle T_{kin} \rangle$, the internal temperature $\langle T_{int} \rangle$, the virial pressure $\langle P_{vir} \rangle$, and the particle density $\langle \rho \rangle$, determined for Test Case #2 simulations of the pure and equimolar binary DPD fluids. T_{bar} is the Langevin barostat temperature and $\langle \cdot \rangle$ denotes an ensemble average, where numbers in parentheses are uncertainties calculated from block averages.	20
Table 5. The kinetic temperature $\langle T_{kin} \rangle$, the internal temperature $\langle T_{int} \rangle$, the virial pressure $\langle P_{vir} \rangle$, and the mass density $\langle \rho \rangle$, determined for Test Case #2 simulations of the coarse-grain solid model of nickel. T_{bar} is the Langevin barostat temperature and $\langle \cdot \rangle$ denotes an ensemble average, where numbers in parentheses are uncertainties calculated from block averages.	23
Table A-1. The configurational energy per particle $\langle u \rangle$, the kinetic temperature $\langle T_{kin} \rangle$, the internal temperature $\langle T_{int} \rangle$, the virial pressure $\langle P_{vir} \rangle$, the particle density $\langle \rho \rangle$, the isentropic compressibility κ_s , and the volume fluctuation δV^2 for the DPD fluid at various values of the Langevin barostat temperature, T_{bar} . $\langle \cdot \rangle$ denotes an ensemble average, where numbers in parentheses are uncertainties calculated from block averages. These simulations were all started from the same final configuration of a constant-temperature DPD simulation at $T = 1$ and particle density $\rho = 3$. The imposed pressure $P_0 = 23.65$ corresponds to $\langle P_{vir} \rangle$ from the constant-temperature DPD simulation. Since $C_v / k_B = 60$ was used in the coarse-grain particle equation-of-state, equilibrium temperatures should be $1 - k_B / C_v \cong 0.983$; C_v is the heat capacity.	32

Acknowledgments

Martin Lísal acknowledges that this research was sponsored by the U.S. Army Research Laboratory (ARL) and was accomplished under cooperative agreement number W911NF-10-2-0039. The views and conclusions contained in this document are those of the authors and should not be interpreted as representing the official policies, either expressed or implied, of ARL or the U.S. government. The U.S. government is authorized to reproduce and distribute reprints for government purposes notwithstanding any copyright notation herein. John K. Brennan acknowledges support in part by the Office of Naval Research and the Department of Defense High-Performance Computing Modernization Program Software Application Institute for Multiscale Reactive Modeling of Insensitive Munitions.

1. Introduction

Extensions of the original constant-temperature Dissipative Particle Dynamics (DPD) method have been developed; in particular, methods that impose constant-energy (DPD-E) (1, 2) and constant-pressure (DPD-P) (3, 4) conditions. An extension not currently available within the DPD framework is an approach that imposes constant-enthalpy conditions (DPD-H). While conserving total enthalpy, such an approach would allow temperature variations within the simulation cell under constant-pressure conditions. Analogous to applications of constant-enthalpy molecular dynamics (MD), DPD-H can be applied to pressure-dependent nonequilibrium conditions, e.g., where mixing becomes prohibitive as the simulation cell pressure increases for diffusion-limited phenomena (5). As part of the work presented here, we develop a DPD-H method by combining the equations of motion (EOM) for a barostat with the EOM for the DPD-E method. Both deterministic (Hoover) and stochastic (Langevin) barostats are implemented within the DPD-H formulation, where a *barostat temperature* is defined to satisfy the fluctuation-dissipation theorem (FDT) for the Langevin barostat.

When applying any DPD variant, numerical integration of the EOM is a key consideration because the stochastic component requires special attention. Recent work by our group (6–8) has provided a comprehensive description of numerical integration schemes based upon the Shardlow-splitting algorithm (SSA) (9) for the isothermal, isothermal-isobaric, and isoenergetic DPD methods. The SSA decomposes the EOM into differential equations that correspond to the deterministic dynamics, and elementary stochastic differential equations (SDEs) that correspond to the stochastic dynamics. In the original SSA formulation, both types of differential equations are integrated via the velocity-Verlet algorithm (9), where the stochastic dynamics are additionally solved in an implicit manner that conserves linear momentum.

In this work, we provide an SSA formulation for the DPD-H method, which is verified by considering both the standard DPD fluid (pure and binary mixtures) (10) and a coarse-grain solid model (11). For both models, we further verify the DPD-H variant by instantaneously heating a slab of particles in the simulation cell. We monitor the evolution of the temperature, pressure, and density as the system approaches an equilibrated state while maintaining constant-enthalpy conditions. For completeness, derivations of the Fokker-Planck equation (FPE) and the FDT for the DPD-H variant are included in appendix A.

2. Formulations of DPD at Fixed Pressure and Enthalpy Using Shardlow-Like Splitting Numerical Discretization

2.1 General Formulation of DPD

DPD particles are defined by a mass m_i , position \mathbf{r}_i , and momentum \mathbf{p}_i . The particles interact with each other via a pair-wise force \mathbf{F}_{ij} that is written as the sum of a conservative force \mathbf{F}_{ij}^C , dissipative force \mathbf{F}_{ij}^D , and random force \mathbf{F}_{ij}^R :

$$\mathbf{F}_{ij} = \mathbf{F}_{ij}^C + \mathbf{F}_{ij}^D + \mathbf{F}_{ij}^R. \quad (1)$$

\mathbf{F}_{ij}^C is given as the negative derivative of a coarse-grain potential, u_{ij}^{CG} , expressed as

$$\mathbf{F}_{ij}^C = -\frac{du_{ij}^{CG}}{dr_{ij}} \frac{\mathbf{r}_{ij}}{r_{ij}} \quad (2)$$

where $\mathbf{r}_{ij} = \mathbf{r}_i - \mathbf{r}_j$ is the separation vector between particle i and particle j , and $r_{ij} = |\mathbf{r}_{ij}|$. The remaining two forces, \mathbf{F}_{ij}^D and \mathbf{F}_{ij}^R , can be interpreted as a means to compensate for the degrees of freedom neglected by coarse-graining. The conservative force is not specified by the DPD formulation and can be chosen to include any forces that are appropriate for a given application, including multibody interactions (e.g., 11–13). \mathbf{F}_{ij}^D and \mathbf{F}_{ij}^R are defined as

$$\mathbf{F}_{ij}^D = -\gamma_{ij} \omega^D(r_{ij}) \left(\frac{\mathbf{r}_{ij}}{r_{ij}} \cdot \mathbf{v}_{ij} \right) \frac{\mathbf{r}_{ij}}{r_{ij}} \quad (3)$$

and

$$\mathbf{F}_{ij}^R = \sigma_{ij} \omega^R(r_{ij}) W_{ij} \frac{\mathbf{r}_{ij}}{r_{ij}}, \quad (4)$$

where γ_{ij} and σ_{ij} are the friction coefficient and noise amplitude between particle i and particle j , respectively, $\mathbf{v}_{ij} = \frac{\mathbf{p}_i}{m_i} - \frac{\mathbf{p}_j}{m_j}$, and W_{ij} are independent Wiener processes such that $W_{ij} = W_{ji}$.

The weight functions $\omega^D(r)$ and $\omega^R(r)$ vanish for $r \geq r_c$, where r_c is the cutoff radius. Note that \mathbf{F}_{ij}^C is completely independent of \mathbf{F}_{ij}^D and \mathbf{F}_{ij}^R , while \mathbf{F}_{ij}^D and \mathbf{F}_{ij}^R are not independent but rather coupled through a fluctuation-dissipation relation. This coupling arises from the requirement that in the thermodynamic limit, the system samples the corresponding probability distribution. The necessary conditions can be derived using a FPE, which are derived in appendix A for the DPD-H variant.

2.2 Constant-Enthalpy DPD

We propose a constant-enthalpy DPD variant based upon a combination of the EOM for a barostat (7) and the EOM for DPD-E (8). For uniform dilation, the combined EOM read as

$$\begin{aligned}
d\mathbf{r}_i &= \frac{\mathbf{p}_i}{m_i} dt + \frac{p_\varepsilon}{W_\varepsilon} \mathbf{r}_i dt \\
d\mathbf{p}_i &= \sum_{j \neq i} \mathbf{F}_{ij}^C dt - \gamma_{ij} \omega^D \left(\frac{\mathbf{r}_{ij}}{r_{ij}} \cdot \mathbf{v}_{ij} \right) \frac{\mathbf{r}_{ij}}{r_{ij}} dt + \sigma_{ij} \omega^R \frac{\mathbf{r}_{ij}}{r_{ij}} dW_{ij} \\
&\quad - \left(1 + \frac{d}{N_f} \right) \frac{p_\varepsilon}{W_\varepsilon} \mathbf{p}_i dt \quad (i = 1, \dots, N) \\
d \ln V &= \frac{dp_\varepsilon}{W_\varepsilon} dt \\
dp_\varepsilon &= F_\varepsilon dt \\
du_i^{mech} &= \frac{1}{2} \sum_{j \neq i} \gamma_{ij} \omega^D \left(\frac{\mathbf{r}_{ij}}{r_{ij}} \cdot \mathbf{v}_{ij} \right)^2 dt - \frac{d\sigma_{ij}^2}{2} \left(\frac{1}{m_i} + \frac{1}{m_j} \right) (\omega^R)^2 dt \quad (i = 1, \dots, N) \\
&\quad - \sigma_{ij} \omega^R \left(\frac{\mathbf{r}_{ij}}{r_{ij}} \cdot \mathbf{v}_{ij} \right) dW_{ij} \\
du_i^{cond} &= \sum_{j \neq i} \kappa_{ij} \left(\frac{1}{\theta_i} - \frac{1}{\theta_j} \right) \omega^{Dq} dt + \alpha_{ij} \omega^{Rq} dW_{ij}^q, \quad (5)
\end{aligned}$$

where $F_\varepsilon = dV(P - P_0) + \frac{d}{N_f} \sum_i \frac{\mathbf{p}_i \cdot \mathbf{p}_i}{m_i} - \gamma_P P_\varepsilon + \sigma_P W_P$, while γ_{ij} , σ_{ij} , κ_{ij} , and α_{ij} , along with the weight functions, are given by the fluctuation-dissipation relations from the DPD-E method (8):

$$\begin{aligned}
\sigma_{ij}^2 &= 2\gamma_{ij} k_B \Theta_{ij} \\
\omega^D(r) &= [\omega^R(r)]^2 \\
\alpha_{ij}^2 &= 2k_B \kappa_{ij} \\
\omega^{Dq}(r) &= [\omega^{Rq}(r)]^2
\end{aligned}, \quad (6)$$

where the relevant temperature is $\Theta_{ij}^{-1} = \frac{1}{2} \left(\frac{1}{\theta_i} + \frac{1}{\theta_j} \right)$, and $\omega^{Dq}(r)$ and $\omega^{Rq}(r)$ can be chosen similar to $\omega^D(r)$ and $\omega^R(r)$, respectively.

Analogous to the DPD-P variant, either a Hoover barostat ($\gamma_p = \sigma_p = 0$) or a Langevin barostat can be invoked. As elaborated in appendix A, the FDT derived from the FPE for the Langevin barostat parameters γ_p and σ_p read as

$$\sigma_p^2 = 2\gamma_p W_\varepsilon k_B T_{bar}, \quad (7)$$

where T_{bar} is the Langevin barostat temperature, which is an additional Langevin barostat parameter taken together with γ_p , σ_p and W_ε .

The system temperature, which is the same as defined in DPD-E, $T = \frac{1}{3Nk_B} \sum_i \frac{\mathbf{p}_i \cdot \mathbf{p}_i}{m_i}$, does not necessarily coincide with the Langevin barostat temperature since the DPD-H variant corresponds to an adiabatic system. More generally, the equilibrium state (and its fluctuations) of an adiabatic piston in contact with a volume reservoir is a thermodynamically ill-defined problem. Effectively, the equilibrium of the system is achieved through irreversible processes (i.e., where no connection with an external reversible-work device such as a Hoover barostat exists) that depend upon the dissipative processes occurring in both the heat reservoir and in the system (14). Consequently, the Langevin barostat parameters given in equation (7), the system compressibility, and the system viscosity determine the amplitude of the volume fluctuations, and thus the amplitude of the system's energy fluctuations. When T_{bar} is set equal to the system temperature, the equilibrium state (as well as its fluctuations) are identical with those obtained by the Hoover barostat. The effect of the value of T_{bar} on the system properties is presented in table A-1 and figure A-1 of appendix A.

Interestingly, since the Hoover barostat corresponds to the coupling of the system to a volume reservoir through a reversible mechanical device, the volume reservoir is neither associated with a barostat temperature nor does it produce any thermal perturbations on the system. Rather, the fluctuations of the system volume itself are due solely to thermal perturbations caused by the motions of the particles, and thus the system volume fluctuations are independent of W_ε .

In the following, we demonstrate that the EOM for the Hoover barostat conserves the total enthalpy, $H = E + P_0V$. Analogous to constant-enthalpy MD (15), DPD-H with the Hoover barostat should also conserve the quantity

$$\begin{aligned} H' &= H + \frac{p_\varepsilon^2}{2W_\varepsilon} \\ &= E + P_0V + \frac{p_\varepsilon^2}{2W_\varepsilon}, \quad (8) \\ &= \sum_i \frac{\mathbf{p}_i \cdot \mathbf{p}_i}{2m_i} + \sum_i \sum_{j>i} u_{ij}^{CG} + \sum_i u_i^{mech} + \sum_i u_i^{cond} + P_0V + \frac{p_\varepsilon^2}{2W_\varepsilon} \end{aligned}$$

i.e., the time derivative of H' should be zero. First, considering the time derivative of E only in equation (8) gives

$$\frac{dE}{dt} = \sum_i \frac{\mathbf{p}_i}{m_i} \cdot \frac{d\mathbf{p}_i}{dt} - \sum_i \mathbf{F}_i^C \cdot \frac{d\mathbf{r}_i}{dt} + \sum_i \frac{d\mathbf{u}_i^{mech}}{dt} + \sum_i \frac{d\mathbf{u}_i^{cond}}{dt}. \quad (9a)$$

Substituting the corresponding equations given in equation 5 into equation 9a, and using

$\sum_i \frac{d\mathbf{u}_i^{cond}}{dt} = 0$ (as a result of $d\mathbf{u}_i^{cond,i-j} = -d\mathbf{u}_j^{cond,i-j}$, cf. equation 11c), and the expression for the

instantaneous pressure $P = \frac{1}{dV} \left(\sum_i \frac{\mathbf{p}_i \cdot \mathbf{p}_i}{m_i} + \sum_i \sum_{j>i} \mathbf{F}_{ij}^C \cdot \mathbf{r}_{ij} \right)$, results in

$$\frac{dE}{dt} = -\frac{p_\varepsilon}{W_\varepsilon} \left(3PV + \frac{d}{N_f} \sum_i \frac{\mathbf{p}_i \cdot \mathbf{p}_i}{m_i} \right). \quad (9b)$$

Substituting equation 9b into

$$\frac{dH'}{dt} = \frac{dE}{dt} + P_0 \frac{dV}{dt} + \frac{p_\varepsilon}{W_\varepsilon} \frac{dp_\varepsilon}{dt} \quad (9c)$$

and using the corresponding equations from equation 5, directly leads to $\frac{dH'}{dt} = 0$, demonstrating that the EOM in equation 5 in the case of the Hoover barostat conserves total system enthalpy.

Numerical discretization of the EOM straightforwardly follows the splitting strategies employed for DPD-P (7) and DPD-E (8). The conservative terms of the deterministic differential equations are identical to the expressions for DPD-P given as

$$\begin{aligned} d\mathbf{r}_i &= \frac{\mathbf{p}_i}{m_i} dt + \frac{p_\varepsilon}{W_\varepsilon} \mathbf{r}_i dt \\ d\mathbf{p}_i &= \sum_{j \neq i} \mathbf{F}_{ij}^C dt - \left(1 + \frac{d}{N_f} \right) \frac{p_\varepsilon}{W_\varepsilon} \mathbf{p}_i dt \quad (i = 1, \dots, N), \\ d \ln V &= \frac{dp_\varepsilon}{W_\varepsilon} dt \\ dp_\varepsilon &= F_\varepsilon dt \end{aligned} \quad (10)$$

while the fluctuation-dissipation terms of the elementary SDEs are identical to the expressions for DPD-E given as

$$\begin{aligned} d\mathbf{p}_i^{i-j} &= -\gamma_{ij} \omega^D \left(\frac{\mathbf{r}_{ij}}{r_{ij}} \cdot \mathbf{v}_{ij} \right) \frac{\mathbf{r}_{ij}}{r_{ij}} dt + \sigma_{ij} \omega^R \frac{\mathbf{r}_{ij}}{r_{ij}} dW_{ij} \\ d\mathbf{p}_j^{i-j} &= -d\mathbf{p}_i^{i-j} \end{aligned} \quad (11a)$$

$$d\mathbf{u}_i^{\text{mech},i-j} = -\frac{1}{2}d\left(\frac{\mathbf{p}_i^{i-j} \cdot \mathbf{p}_i^{i-j}}{2m_i} + \frac{\mathbf{p}_j^{i-j} \cdot \mathbf{p}_j^{i-j}}{2m_j}\right) \quad \left(\text{for each } i < j\right) \quad (11b)$$

$$d\mathbf{u}_j^{\text{mech},i-j} = d\mathbf{u}_i^{\text{mech},i-j}$$

$$d\mathbf{u}_i^{\text{cond},i-j} = \kappa_{ij}\left(\frac{1}{\theta_i} - \frac{1}{\theta_j}\right)\omega^{Dq}dt + \alpha_{ij}\omega^{Rq}dW_{ij}^q \quad (11c)$$

$$d\mathbf{u}_j^{\text{cond},i-j} = -d\mathbf{u}_i^{\text{cond},i-j}$$

As before, the stochastic flow map $\phi_{\Delta t}$ is approximated from the first-order splitting algorithm given by

$$\phi_{\Delta t} \cong \phi_{\Delta t;1,2}^{\text{diss}} \circ \phi_{\Delta t;1,3}^{\text{diss}} \circ \dots \circ \phi_{\Delta t;i,j}^{\text{diss}} \circ \dots \circ \phi_{\Delta t;N-2,N}^{\text{diss}} \circ \phi_{\Delta t;N-1,N}^{\text{diss}} \circ \phi_{\Delta t}^C, \quad (12)$$

where \circ denotes a composition of operators.

For the Shardlow-splitting algorithm velocity-Verlet (SSA-VV) approach, updates for each $\phi_{\Delta t;i,j}^{\text{diss}}$ term are performed by

$$\begin{aligned} \mathbf{p}_i\left(t + \frac{\Delta t}{2}\right) &= \mathbf{p}_i(t) - \frac{\Delta t}{2}\gamma_{ij}\omega^D\left[\frac{\mathbf{r}_{ij}}{r_{ij}} \cdot \mathbf{v}_{ij}(t)\right]\frac{\mathbf{r}_{ij}}{r_{ij}} + \frac{\sqrt{\Delta t}}{2}\sigma_{ij}\omega^R\zeta_{ij}\frac{\mathbf{r}_{ij}}{r_{ij}} \\ \mathbf{p}_j\left(t + \frac{\Delta t}{2}\right) &= \mathbf{p}_j(t) + \frac{\Delta t}{2}\gamma_{ij}\omega^D\left[\frac{\mathbf{r}_{ij}}{r_{ij}} \cdot \mathbf{v}_{ij}(t)\right]\frac{\mathbf{r}_{ij}}{r_{ij}} - \frac{\sqrt{\Delta t}}{2}\sigma_{ij}\omega^R\zeta_{ij}\frac{\mathbf{r}_{ij}}{r_{ij}} \\ \mathbf{p}_i(t + \Delta t) &= \mathbf{p}_i\left(t + \frac{\Delta t}{2}\right) - \frac{\Delta t}{2}\frac{\gamma_{ij}\omega^D}{1 + \frac{\mu_{ij}}{2}\gamma_{ij}\omega^D\Delta t}\left\{\left[\frac{\mathbf{r}_{ij}}{r_{ij}} \cdot \mathbf{v}_{ij}\left(t + \frac{\Delta t}{2}\right)\right]\frac{\mathbf{r}_{ij}}{r_{ij}} + \sqrt{\Delta t}\frac{\mu_{ij}}{2}\sigma_{ij}\omega^R\zeta_{ij}\frac{\mathbf{r}_{ij}}{r_{ij}}\right\} \\ &\quad + \frac{\sqrt{\Delta t}}{2}\sigma_{ij}\omega^R\zeta_{ij}\frac{\mathbf{r}_{ij}}{r_{ij}} \\ \mathbf{p}_j(t + \Delta t) &= \mathbf{p}_j\left(t + \frac{\Delta t}{2}\right) + \frac{\Delta t}{2}\frac{\gamma_{ij}\omega^D}{1 + \frac{\mu_{ij}}{2}\gamma_{ij}\omega^D\Delta t}\left\{\left[\frac{\mathbf{r}_{ij}}{r_{ij}} \cdot \mathbf{v}_{ij}\left(t + \frac{\Delta t}{2}\right)\right]\frac{\mathbf{r}_{ij}}{r_{ij}} + \sqrt{\Delta t}\frac{\mu_{ij}}{2}\sigma_{ij}\omega^R\zeta_{ij}\frac{\mathbf{r}_{ij}}{r_{ij}}\right\} \\ &\quad - \frac{\sqrt{\Delta t}}{2}\sigma_{ij}\omega^R\zeta_{ij}\frac{\mathbf{r}_{ij}}{r_{ij}} \\ u_i^{\text{cond}}(t + \Delta t) &= u_i^{\text{cond}}(t) + \Delta t\kappa_{ij}\left(\frac{1}{\theta_i} - \frac{1}{\theta_j}\right)\omega^{Dq} + \sqrt{\Delta t}\alpha_{ij}\omega^{Rq}\zeta_{ij}^q \\ u_j^{\text{cond}}(t + \Delta t) &= u_j^{\text{cond}}(t) - \Delta t\kappa_{ij}\left(\frac{1}{\theta_i} - \frac{1}{\theta_j}\right)\omega^{Dq} - \sqrt{\Delta t}\alpha_{ij}\omega^{Rq}\zeta_{ij}^q \end{aligned} \quad (13a)$$

$$\begin{aligned}
\mathbf{u}_i^{mech}(t + \Delta t) &= \mathbf{u}_i^{mech}(t) - \frac{1}{2} \left[\frac{\mathbf{p}_i(t + \Delta t) \cdot \mathbf{p}_i(t + \Delta t)}{2m_i} + \frac{\mathbf{p}_j(t + \Delta t) \cdot \mathbf{p}_j(t + \Delta t)}{2m_j} \right. \\
&\quad \left. - \frac{\mathbf{p}_i(t) \cdot \mathbf{p}_i(t)}{2m_i} - \frac{\mathbf{p}_j(t) \cdot \mathbf{p}_j(t)}{2m_j} \right] \\
\mathbf{u}_j^{mech}(t + \Delta t) &= \mathbf{u}_j^{mech}(t) - \frac{1}{2} \left[\frac{\mathbf{p}_i(t + \Delta t) \cdot \mathbf{p}_i(t + \Delta t)}{2m_i} + \frac{\mathbf{p}_j(t + \Delta t) \cdot \mathbf{p}_j(t + \Delta t)}{2m_j} \right. \\
&\quad \left. - \frac{\mathbf{p}_i(t) \cdot \mathbf{p}_i(t)}{2m_i} - \frac{\mathbf{p}_j(t) \cdot \mathbf{p}_j(t)}{2m_j} \right].
\end{aligned} \tag{13b}$$

In equations 13a and 13b, the superscript $i - j$ is omitted for notational simplicity. Note that the total system energy is exactly conserved via equation 13b. In equation 13a, $\zeta_{ij}^q = -\zeta_{ji}^q$ is a Gaussian random number with zero mean and unit variance, chosen independently for each pair of interacting particles. Finally, $\phi_{\Delta t}^C$ can be approximated by the velocity-Verlet algorithm given by

$$\begin{aligned}
p_\varepsilon\left(t + \frac{\Delta t}{2}\right) &= p_\varepsilon(t) + \frac{\Delta t}{2} F_\varepsilon(t) \\
\varepsilon(t + \Delta t) &= \varepsilon(t) + \Delta t \frac{dp_\varepsilon\left(t + \frac{\Delta t}{2}\right)}{W_\varepsilon} \\
V(t + \Delta t) &= V(0) \exp[\varepsilon(t + \Delta t)] \\
L(t + \Delta t) &= V(t + \Delta t)^{1/3}, \\
\mathbf{p}_i\left(t + \frac{\Delta t}{2}\right) &= \mathbf{p}_i(t) + \frac{\Delta t}{2} \left[\mathbf{F}_i^C(t) - \left(2 + \frac{d}{N_f}\right) \frac{p_\varepsilon(t)}{W_\varepsilon} \mathbf{p}_i(t) \right] \quad (i = 1, \dots, N) \\
\mathbf{r}_i(t + \Delta t) &= \exp[\varepsilon(t + \Delta t) - \varepsilon(t)] \left[\mathbf{r}_i(t) + \Delta t \frac{\mathbf{p}_i\left(t + \frac{\Delta t}{2}\right)}{m_i} \right]
\end{aligned} \tag{14a}$$

where $L(0)$ and $L(t + \Delta t)$ are the lengths of the cubic simulation box at $t = 0$ and $t + \Delta t$, respectively. Next, the conservative forces at $t + \Delta t$, $\{\mathbf{F}_i^C(t + \Delta t)\}_{i=1}^N$, are evaluated and subsequently used in the second part of the algorithm, which requires an iterative approach. The iteration starts with an estimation of p_ε at $t + \Delta t$ using $p_\varepsilon^{(0)}(t + \Delta t) = p_\varepsilon(t - \Delta t) + 2\Delta t F_\varepsilon(t)$, followed by solving the set of equations

$$\begin{aligned}
\mathbf{p}_i^{(k)}(t + \Delta t) &= \frac{\exp[\varepsilon(t + \Delta t) - \varepsilon(t)] \mathbf{p}_i \left(t + \frac{\Delta t}{2} \right) + \frac{\Delta t}{2} \mathbf{F}_i^C(t + \Delta t)}{1 + \frac{\Delta t}{2} \left(2 + \frac{d}{N_f} \right) \frac{p_\varepsilon^{(k-1)}(t + \Delta t)}{W_\varepsilon}} \quad (i = 1, \dots, N) \\
F_\varepsilon^{(k)}(t + \Delta t) &= dV(t + \Delta t) [P^{(k)}(t + \Delta t) - P_0] + \frac{d}{N_f} \sum_i \frac{\mathbf{p}_i^{(k)}(t + \Delta t) \cdot \mathbf{p}_i^{(k)}(t + \Delta t)}{m_i} \\
&\quad - \gamma_P p_\varepsilon^{(k-1)}(t + \Delta t) + \sigma_P \frac{\zeta_P}{\sqrt{\Delta t}} \\
p_\varepsilon^{(k)}(t + \Delta t) &= p_\varepsilon \left(t + \frac{\Delta t}{2} \right) + \frac{\Delta t}{2} F_\varepsilon^{(k)}(t + \Delta t)
\end{aligned} \tag{14b}$$

self-consistently until $\left| \frac{\sum_i [\mathbf{p}_i^{(k)}(t + \Delta t) - \mathbf{p}_i^{(k-1)}(t + \Delta t)]^2}{3N} \right|$ is less than a prescribed tolerance, which

is typically less than 10^{-6} . In equation 14b, ζ_P is a Gaussian random number with zero mean and unit variance and (k) is the iteration index.

A practical implementation of the SSA-VV for DPD-H follows. The EOM and the numerical discretization for nonuniform dilation are also presented in appendix B.

1. Stochastic Integration for all $i - j$ pairs of particles

- (i) $\mathbf{p}'_i \leftarrow \mathbf{p}_i, \mathbf{p}'_j \leftarrow \mathbf{p}_j$
- (ii) $\mathbf{p}_i \leftarrow \mathbf{p}_i - \frac{\Delta t}{2} \gamma_{ij} \omega^D \left(\frac{\mathbf{r}_{ij}}{r_{ij}} \cdot \mathbf{v}_{ij} \right) \frac{\mathbf{r}_{ij}}{r_{ij}} + \sigma_{ij} \omega^R \zeta_{ij} \frac{\mathbf{r}_{ij}}{r_{ij}} \frac{\sqrt{\Delta t}}{2}$
- (iii) $\mathbf{p}_j \leftarrow \mathbf{p}_j + \frac{\Delta t}{2} \gamma_{ij} \omega^D \left(\frac{\mathbf{r}_{ij}}{r_{ij}} \cdot \mathbf{v}_{ij} \right) \frac{\mathbf{r}_{ij}}{r_{ij}} - \sigma_{ij} \omega^R \zeta_{ij} \frac{\mathbf{r}_{ij}}{r_{ij}} \frac{\sqrt{\Delta t}}{2}$
- (iv) $\mathbf{v}_{ij} \leftarrow \frac{\mathbf{p}_i - \mathbf{p}_j}{m_i - m_j}$
- (v) $\mathbf{p}_i \leftarrow \mathbf{p}_i - \frac{\Delta t}{2} \frac{\gamma_{ij} \omega^D}{1 + \frac{\mu_{ij}}{2} \gamma_{ij} \omega^D \Delta t} \left[\left(\frac{\mathbf{r}_{ij}}{r_{ij}} \cdot \mathbf{v}_{ij} \right) \frac{\mathbf{r}_{ij}}{r_{ij}} + \frac{\mu_{ij}}{2} \sigma_{ij} \omega^R \zeta_{ij} \frac{\mathbf{r}_{ij}}{r_{ij}} \sqrt{\Delta t} \right] + \sigma_{ij} \omega^R \zeta_{ij} \frac{\mathbf{r}_{ij}}{r_{ij}} \frac{\sqrt{\Delta t}}{2}$
- (vi) $\mathbf{p}_j \leftarrow \mathbf{p}_j + \frac{\Delta t}{2} \frac{\gamma_{ij} \omega^D}{1 + \frac{\mu_{ij}}{2} \gamma_{ij} \omega^D \Delta t} \left[\left(\frac{\mathbf{r}_{ij}}{r_{ij}} \cdot \mathbf{v}_{ij} \right) \frac{\mathbf{r}_{ij}}{r_{ij}} + \frac{\mu_{ij}}{2} \sigma_{ij} \omega^R \zeta_{ij} \frac{\mathbf{r}_{ij}}{r_{ij}} \sqrt{\Delta t} \right] - \sigma_{ij} \omega^R \zeta_{ij} \frac{\mathbf{r}_{ij}}{r_{ij}} \frac{\sqrt{\Delta t}}{2}$
- (vii) $u_i^{cond} \leftarrow u_i^{cond} + \kappa_{ij} \left(\frac{1}{\theta_i} - \frac{1}{\theta_j} \right) \omega^{Dq} \Delta t + \alpha_{ij} \omega^{Rq} \zeta_{ij}^q \sqrt{\Delta t}$

$$(viii) u_j^{cond} \leftarrow u_j^{cond} - \kappa_{ij} \left(\frac{1}{\theta_i} - \frac{1}{\theta_j} \right) \omega^{Dq} \Delta t - \alpha_{ij} \omega^{Rq} \zeta_{ij}^q \sqrt{\Delta t}$$

$$(ix) u_i^{mech} \leftarrow u_i^{mech} - \frac{1}{2} \left[\frac{\mathbf{p}_i \cdot \mathbf{p}_i}{2m_i} + \frac{\mathbf{p}_j \cdot \mathbf{p}_j}{2m_j} - \frac{\mathbf{p}'_i \cdot \mathbf{p}'_i}{2m_i} - \frac{\mathbf{p}'_j \cdot \mathbf{p}'_j}{2m_j} \right]$$

$$(x) u_j^{mech} \leftarrow u_j^{mech} - \frac{1}{2} \left[\frac{\mathbf{p}_i \cdot \mathbf{p}_i}{2m_i} + \frac{\mathbf{p}_j \cdot \mathbf{p}_j}{2m_j} - \frac{\mathbf{p}'_i \cdot \mathbf{p}'_i}{2m_i} - \frac{\mathbf{p}'_j \cdot \mathbf{p}'_j}{2m_j} \right]$$

2. Deterministic Integration #1.1

$$(i) p_\varepsilon \left(t + \frac{\Delta t}{2} \right) = p_\varepsilon(t) + \frac{\Delta t}{2} F_\varepsilon(t)$$

$$(ii) \varepsilon(t + \Delta t) = \varepsilon(t) + \Delta t \frac{dp_\varepsilon \left(t + \frac{\Delta t}{2} \right)}{W_\varepsilon}$$

$$(iii) V(t + \Delta t) = V(0) \exp[\varepsilon(t + \Delta t)]$$

$$(iv) L(t + \Delta t) = V(t + \Delta t)^{1/3}$$

3. Deterministic Integration #1.2 for $i = 1, \dots, N$

$$(i) \mathbf{p}_i \left(t + \frac{\Delta t}{2} \right) = \mathbf{p}_i(t) + \frac{\Delta t}{2} \left[\mathbf{F}_i^C(t) - \left(2 + \frac{d}{N_f} \right) \frac{p_\varepsilon(t)}{W_\varepsilon} \mathbf{p}_i(t) \right]$$

$$(ii) \mathbf{r}_i(t + \Delta t) = \exp[\varepsilon(t + \Delta t) - \varepsilon(t)] \left[\mathbf{r}_i(t) + \Delta t \frac{\mathbf{p}_i \left(t + \frac{\Delta t}{2} \right)}{m_i} \right]$$

4. Conservative Force Calculation: $\{\mathbf{F}_i^C\}_{i=1}^N$

3. Computational Details

The SSA-VV for the DPD-H variant was tested using both the standard DPD fluid (10) and a coarse-grain solid model (11), where complete details of the conservative forces for these models are given in appendix C. Both a pure component case and an equimolar binary mixture were tested for the DPD fluid model. System sizes for the DPD fluids and coarse-grain solid were, respectively, $N = 10125$ and 13500. For these simulations, the following reduced units were used: r_c and r_0 are the unit of length for the DPD fluid and coarse-grain solid, respectively; the mass of a DPD particle is the unit of mass; and the unit of energy is $k_B T_{ini}$, where T_{ini} is the initial system temperature. Using these reduced units, we set the maximum repulsion between

particles i and j as $a_{ij} = 25$ for the pure DPD fluid, and as $a_{ij} = 25$ and 28 for the like and unlike $i - j$ interactions, respectively, for the binary DPD fluid. Further, we set the noise amplitude $\sigma_{ij} = 3$, and the barostat characteristic time $\tau_p = 2$. Prescriptions for the choice of γ_p (3, 16) suggest that the value should be between $2/\tau_p$ and $10/\tau_p$; therefore, we set $\gamma_p = 10/\tau_p = 5$. Next, we assume that the internal degrees of freedom are purely harmonic and express the coarse-grain particle equation of state as $u_i = C_{v,i}\theta_i$, with heat capacity $C_{v,i}/k_B \equiv C_v/k_B = 60$ and 48 for the pure DPD fluid and coarse-grain solid, respectively. Note that these values correspond to coarse-graining approximately 20 atoms and, separately, 16 atoms into a DPD particle, respectively (17). For the binary DPD fluid, we set $m_2 = 10m_1$ and $C_{v,2} = 10C_{v,1}$, where $C_{v,1}/k_B = 60$. Finally, following Ripoll et al. (18), the mesoscopic thermal conductivity κ_{ij} is chosen as

$$\kappa_{ij} = \kappa_0 \frac{C_v^2}{4k_B} (\theta_i + \theta_j)^2, \quad (15)$$

where κ_0 is the parameter controlling the thermal conductivity of the DPD particles, which are chosen as $\kappa_0 = 2.80 \cdot 10^{-4}$ for the pure DPD fluid and $\kappa_0 = 1.52 \cdot 10^{-4}$ for the coarse-grain solid. For the binary fluid, we set $\kappa_{0,11} = 2.80 \cdot 10^{-4}$, $\kappa_{0,22} = 2.80 \cdot 10^{-6}$, and $\kappa_{0,12} = \sqrt{\kappa_{0,11}\kappa_{0,22}}$. Note that when $\theta_i = \theta_j = 1$, these particular values of κ_0 and C_v give $\kappa_{ij} = 1$.

4. Results

The results section is organized as follows. The validity of the SSA integration algorithm for the DPD-H variant is verified by considering equilibrium and nonequilibrium scenarios, where results are given in subsections 1 and 2, respectively. Finally, we briefly review the energy drift associated with finite integration methods and propose a simple strategy to minimize these drifts in DPD-H simulations.

4.1 Test Case No. 1: Equivalence of DPD Variants

As a first test of the SSA-VV formulation for the DPD-H variant, we verify that it converges to the same equilibrium properties when at the same thermodynamic conditions as other DPD variants. Starting from an equilibrated configuration from a constant-temperature DPD simulation, DPD-P, DPD-E, and DPD-H simulations were performed at imposed values of P , E , and H , respectively, where these values were determined from the constant-temperature DPD simulation.

4.1.1 DPD Fluid

The benchmark systems for both the pure and binary DPD fluid cases are taken from a constant-temperature DPD simulation performed at $\rho = 3$ and $T = 1$, and run for $t_{run} = 3000$ and $\Delta t = 0.03$. Further, DPD-P simulations were performed using both the Langevin and Hoover

barostats with an imposed pressure determined from the constant-temperature DPD simulation ($P_0 = 23.65$ and $P_0 = 24.79$ for the pure and equimolar binary DPD fluids, respectively) for $t_{run} = 3000$ and $\Delta t = 0.03$. The following quantities were evaluated and are listed in table 1 (pure fluid) and table 2 (equimolar binary fluid): virial pressure $\langle P_{vir} \rangle$, configurational energy per particle $\langle u \rangle$, kinetic temperature $\langle T_{kin} \rangle$, and self-diffusion coefficients D using the Einstein relation (15).

Table 1. The configurational energy per particle $\langle u \rangle$, the kinetic temperature $\langle T_{kin} \rangle$, the internal temperature $\langle T_{int} \rangle$, the virial pressure $\langle P_{vir} \rangle$, the particle density $\langle \rho \rangle$, and the self-diffusion coefficient D , determined from test case no. 1 simulations of the pure DPD fluid. T_{bar} is the Langevin barostat temperature and $\langle \cdot \rangle$ denotes an ensemble average, where numbers in parentheses are uncertainties calculated from block averages.

Variant	$\langle u \rangle$	$\langle T_{kin} \rangle$	$\langle T_{int} \rangle$	$\langle P_{vir} \rangle$	$\langle \rho \rangle$	D
DPD $\rho = 3$	4.56(1)	1.005(8)	—	23.65(8)	—	0.295(13)
DPD-P Langevin $P_0 = 23.65$	4.55(1)	1.005(8)	—	23.59(8)	2.997(8)	0.294(14)
DPD-P Hoover $P_0 = 23.65$	4.55(1)	1.004(8)	—	23.61(8)	2.997(8)	0.296(19)
DPD-E $\rho = 3$	4.54(1)	0.985(8)	0.985(3)	23.61(11)	—	0.293(6)
DPD-H Langevin $T_{bar} = 1.0$ $P_0 = 23.65$	4.54(2)	0.985(8)	0.985(3)	23.65(11)	3.002(11)	0.294(7)
DPD-H Hoover $P_0 = 23.65$	4.54(2)	0.986(8)	0.985(3)	23.65(9)	3.002(13)	0.292(8)

Table 2. The configurational energy per particle $\langle u \rangle$, the kinetic temperature $\langle T_{kin} \rangle$, the internal temperature $\langle T_{int} \rangle$, the virial pressure $\langle P_{vir} \rangle$, the particle density $\langle \rho \rangle$, and the self-diffusion coefficient D , determined from test case no. 1 simulations of the equimolar binary DPD fluid. T_{bar} is the Langevin barostat temperature and $\langle \cdot \rangle$ denotes an ensemble average, where numbers in parentheses are uncertainties calculated from block averages.

Variant	$\langle u \rangle$	$\langle T_{kin} \rangle$	$\langle T_{int} \rangle$	$\langle P_{vir} \rangle$	$\langle \rho \rangle$	D_1	D_2
DPD $\rho = 3$	4.76(1)	1.005(8)	—	24.79(13)	—	0.177(13)	0.165(13)
DPD-P Langevin $P_0 = 24.79$	4.76(2)	1.004(8)	—	24.76(4)	2.998(8)	0.176(15)	0.163(17)
DPD-P Hoover $P_0 = 24.79$	4.76(1)	1.004(8)	—	24.75(4)	2.998(9)	0.179(12)	0.165(9)
DPD-E $\rho = 3$	4.75(1)	0.993(8)	0.994(3)	24.77(21)	—	0.174(9)	0.161(10)
DPD-H Langevin $T_{bar} = 1.0$ $P_0 = 24.79$	4.75(2)	0.992(8)	0.994(3)	24.78(13)	3.001(9)	0.174(8)	0.160(9)
DPD-H Hoover $P_0 = 24.79$	4.75(2)	0.993(8)	0.994(3)	24.78(19)	3.001(13)	0.173(8)	0.160(10)

To validate the constant-enthalpy SSA-VV formulation, DPD-H simulations were performed at conditions taken from the constant-temperature DPD simulation, i.e., $V = L^3 = 3375$ (L is the box length) and $P_0 = 23.65$ or $P_0 = 24.79$ for the pure and equimolar binary fluids, respectively. DPD-H simulations were carried out using both the Langevin and Hoover barostats, where $T_{bar} = 1$ was used for the Langevin barostat. The final configuration of the constant-temperature DPD simulation is used to determine the imposed value of H , thus it is also used as the starting configuration for the DPD-H simulation. The values of u_i were initialized by setting $u_i = C_{v,i} T_{ini}$, where $T_{ini} = T = 1$, and were carried out for $t_{run} = 3000$ and $\Delta t = 0.01$. Analogous to isoenthalpic MD simulations, the use of a smaller Δt , with respect to constant-temperature DPD or DPD-P simulations, is required for proper conservation of H' . Using $\Delta t = 0.01$, we observed a relative drift in H' no higher than $1 \cdot 10^{-4}$. (For the DPD fluid simulations, reported relative drifts refer to an average of relative drifts over time periods of 1000.)

Comparing the DPD-E (8) and DPD-H results with the constant-temperature DPD and DPD-P results in tables 1 and 2, excellent overall agreement is found. For the DPD-H simulation, the internal temperature, $\langle T_{int} \rangle = \left\langle \frac{1}{N} \sum_{i=1}^N \frac{1}{\theta_i} \right\rangle^{-1}$ was also evaluated, where the values of $\langle T_{kin} \rangle$ and $\langle T_{int} \rangle$ agree within statistical uncertainties. For the pure DPD fluid, these values are approximately 1.5% lower than $T_{ini} = 1$; however, this discrepancy is due to the fundamental differences

between the constant-temperature DPD and DPD-E/DPD-H methods. Effectively, the two systems are different since the imposed temperature for the constant-temperature DPD system should be equivalent to $\langle T_{kin} \rangle$, while in the DPD-E/DPD-H system the total energy initially given to the system is dynamically partitioned among the kinetic and internal energies, yielding a variation in the equilibrium temperature with respect to T_{ini} (19). This difference is of $O(k_B/C_v)$ as compared with unity, while an additional contribution of the same order arises from the “extra degree of freedom” due to the fluctuations in u_i , since the relevant macroscopic temperature is related to $\left(\frac{1}{\theta_i}\right)^{-1}$. Hence, for a pure DPD fluid up to first order in k_B/C_v ,

$\langle T_{kin} \rangle = \langle T_{int} \rangle \cong T_{ini}(1 - k_B/C_v) \cong 0.983$ (19), in agreement with the simulated values of 0.985 ± 0.003 . For the equimolar binary fluid, the simulated values are also in agreement with the estimate $\langle T_{kin} \rangle = \langle T_{int} \rangle \cong 0.994$. Note that the estimated value is closer to $T_{ini} = 1$ due to the larger value of $C_{v,2}$ that reduces the (k_B/C_v) contribution. Due to these lower values of $\langle T_{kin} \rangle$ and $\langle T_{int} \rangle$, the values of $\langle \rho \rangle$ for DPD-H in tables 1 and 2 differ slightly from $\langle \rho \rangle$ for DPD-P.

Reproducing equilibrium averages is necessary but not sufficient proof that the integration scheme is behaving properly. Hence, as a further demonstration of the quality of the SSA-VV and the proper choice of Δt , for the pure DPD fluid, we calculated probability distributions for p_i , u_i , and V for constant-temperature DPD and DPD-P with $\Delta t = 0.03$, and for DPD-H with $\Delta t = 0.01$. We compared the probability distribution for p_i with the corresponding Maxwell-Boltzmann distribution (15), while the probability distributions for u_i and V were compared with those obtained with a very small $\Delta t = 0.001$, which is more than an order of magnitude smaller than typical values of Δt used and is thus approximated as the “exact” result. As an example of results, figure 1 presents the probability distributions of p_i , u_i , and V for DPD-H using the Langevin barostat, where agreement is excellent.

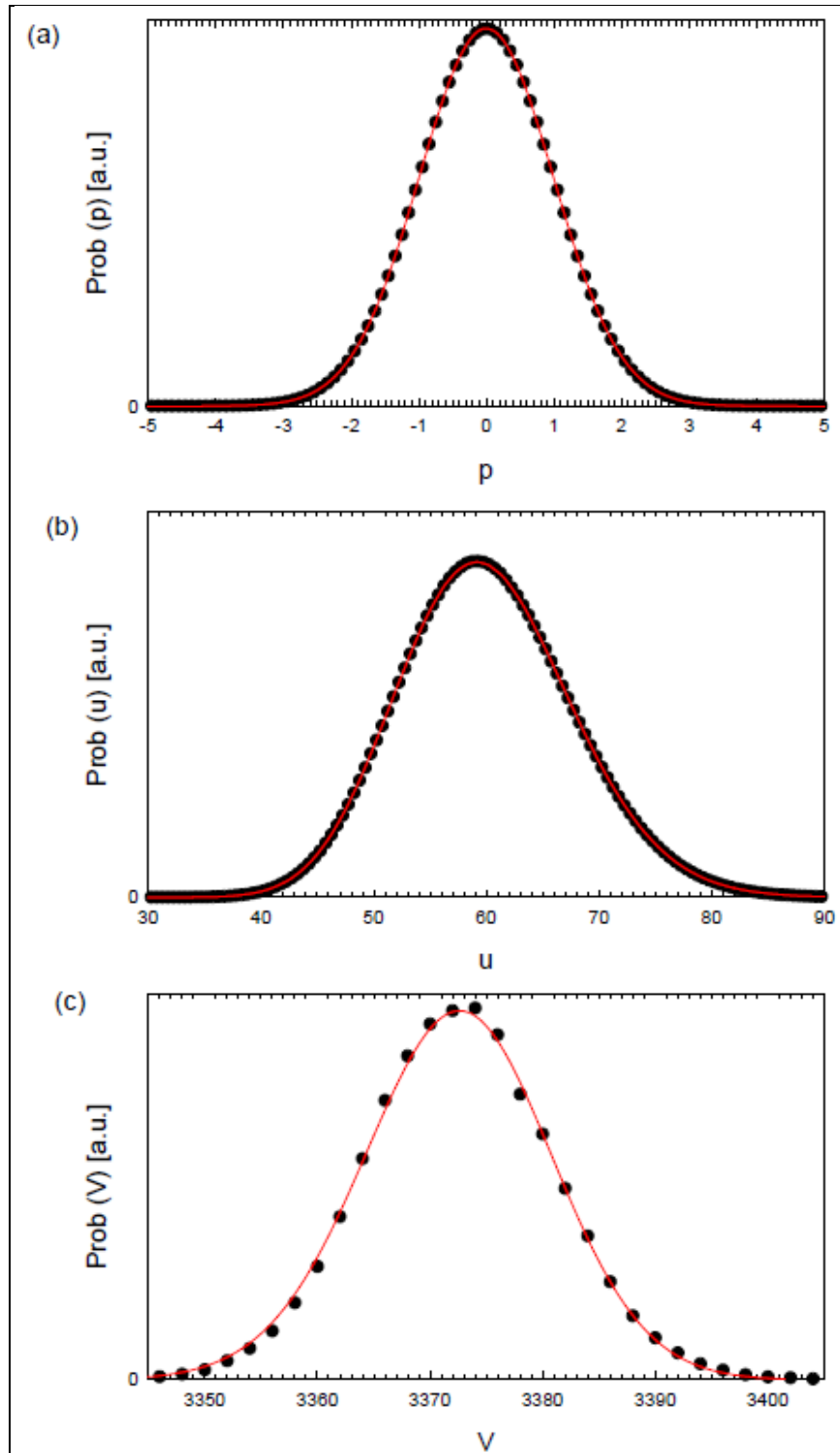


Figure 1. The probability distributions of (a) p_i , (b) u_i , and (c) V for DPD-H with a Langevin barostat. Symbols represent simulation results for $\Delta t = 0.01$, and lines correspond to (a) the Maxwell-Boltzmann distribution for p_i and (b, c) “exact” results, i.e., simulation results where $\Delta t = 0.001$.

4.1.2 Coarse-Grain Solid

A validation study analogous to the DPD fluids study is performed for a coarse-grain solid model, where a recently developed nickel model is considered that reasonably reproduces several measured properties, including the melting temperature (11). For a benchmark system, a constant-temperature DPD simulation is performed at $\rho = 8260 \text{ kg/m}^3$ and $T = 1300 \text{ K}$ for $t_{run} = 1 \text{ ns}$ and $\Delta t = 5 \text{ fs}$, where results are listed in table 3. At this state point, the atomistic Sutton-Chen (SC) model of nickel predicts a pressure of approximately 0 bar (11), while $\langle P_{vir} \rangle$ for the coarse-grain solid model is larger than 0 bar. Next, starting from an equilibrated configuration from a constant-temperature DPD simulation, nonuniform dilation DPD-P simulations were performed using both the Langevin and Hoover barostats at $P_0 = 0 \text{ bar}$ for $t_{run} = 1 \text{ ns}$ and $\Delta t = 5 \text{ fs}$, where results are also shown in table 3.

Table 3. The molar configurational energy $\langle u \rangle$, the kinetic temperature $\langle T_{kin} \rangle$, the internal temperature $\langle T_{int} \rangle$, the virial pressure $\langle P_{vir} \rangle$, and the mass density $\langle \rho \rangle$ determined from test case no. 1 simulations of the coarse-grain solid model of nickel. T_{bar} is the Langevin barostat temperature and $\langle \cdot \rangle$ denotes an ensemble average, where numbers in parentheses are uncertainties calculated from block averages.

Variant	$\langle u \rangle$ (kJ/mol)	$\langle T_{kin} \rangle$ (K)	$\langle T_{int} \rangle$ (K)	$\langle P_{vir} \rangle$ (bar)	$\langle \rho \rangle$ (kg/m ³)
DPD $\rho = 8260 \text{ kg/m}^3$	-508.44(11)	1300.1(91)	—	5.91(94)	—
DPD-P Langevin $P_0 = 0 \text{ bar}$	-508.43(14)	1299.9(92)	—	-0.13(95)	8259.3(73)
DPD-P Hoover $P_0 = 0 \text{ bar}$	-508.44(14)	1299.7(91)	—	0.06(99)	8260.1(68)
DPD-E $\rho = 8260 \text{ kg/m}^3$	-508.71(11)	1274.8(88)	1274.5(5)	-150.49(98)	—
DPD-H Langevin $T_{bar} = 1300 \text{ K}$ $P_0 = 0 \text{ bar}$	-508.86(14)	1276.1(89)	1275.7(11)	-0.27(97)	8273.2(73)
DPD-H Hoover $P_0 = 0 \text{ bar}$	-508.87(13)	1275.8(89)	1275.6(5)	0.07(986)	8273.9(80)

Analogous to the DPD fluid study, DPD-H simulations were performed at conditions determined from the constant-temperature DPD simulation, specifically, $P_0 = 0$ bar. The value of H imposed in the DPD-H simulation was determined from the final configuration of the constant-temperature DPD simulation, which is used as the starting configuration. The value of u_i was initialized by setting $u_i = C_V T_{ini}$, where $T_{ini} = T = 1300$ K. Nonuniform dilation DPD-H simulations were carried out using both the Langevin and Hoover barostats, with $T_{bar} = 1300$ K for the Langevin barostat. All simulations were run for $t_{run} = 1$ ns and $\Delta t = 5$ fs, where a relative drift in H' under $2 \cdot 10^{-4}$ was observed. (For the coarse-grain solid simulations, reported relative drifts refer to an average of relative drifts over time periods of 1 ns.) Comparing the DPD-E (8) and DPD-H results with the constant-temperature DPD and DPD-P results in table 3, excellent overall agreement is found. For both DPD-E and DPD-H, the values of $\langle T_{kin} \rangle$ and $\langle T_{int} \rangle$ are equal within statistical uncertainties. These values are approximately 2% lower than $T_{ini} = 1300$ K but agree within statistical uncertainties when the extra degree of freedom due to the fluctuations in u_i is considered, i.e., $\langle T_{kin} \rangle = \langle T_{int} \rangle \cong T_{ini} (1 - k_B / C_V) \cong 1273$ K (19). Furthermore, due to these lower values of $\langle T_{kin} \rangle$ and $\langle T_{int} \rangle$, the values of $\langle P_{vir} \rangle$ for DPD-E and $\langle \rho \rangle$ for DPD-H in table 3 differ accordingly from $\langle P_{vir} \rangle$ and $\langle \rho \rangle$ for constant-temperature DPD and DPD-P, respectively.

4.2 Test Case No. 2: Heating Response in DPD-H Simulations

As a second test case to verify the SSA-VV formulation for the DPD-H variant, a nonequilibrium scenario was considered for both the DPD fluids and the coarse-grain solid model. Starting from a final configuration of a constant-temperature DPD simulation, a slab of DPD particles in the middle of the simulation box was instantaneously heated and the system response was studied at constant- (P, H) conditions, i.e., by DPD-H simulations.

4.2.1 DPD Fluid

Analogous to test case no. 1, the final configuration from the constant-temperature DPD simulation (at $T = 1$ and $\rho = 3$) was used as the starting configuration. For this configuration, a slab of particles of width $0.5L$ in the middle of the simulation box was heated by assigning velocities from a Maxwell-Boltzmann distribution corresponding to T_{heat} , and by setting $u_i = C_{V,i} T_{heat}$. The remaining (nonheated) particles were assigned $u_i = C_{V,i} T_{ini}$, where $T_{ini} = T = 1$.

As a test of the DPD-H variant with the Langevin and Hoover barostats, a simulation was performed using $T_{heat} = 10$ and $P_0 = 23.65$ (pure fluid) or $P_0 = 24.79$ (equimolar binary fluid) for $t_{run} = 5000$ and $\Delta t = 0.005$ (the value of P_0 corresponds to the pressure determined from the constant-temperature DPD simulation at $T = 1$ and $\rho = 3$). $T_{bar} = T_{ini}$ was used for the Langevin barostat. The time evolutions of T_{kin} , T_{int} , P_{vir} , and ρ for the pure DPD fluid are shown in figure 2, where a relative drift of $6 \cdot 10^{-5}$ in H' was observed. As evident in figures 2a and 2b, rapid equalization of T_{kin} and T_{int} was observed, followed by increasing T_{kin} and T_{int} with t , until reaching equilibrium at $t > 600$. Comparing the performance of the Langevin and Hoover barostats, the Hoover barostat exhibits substantial oscillations in P_{vir} and ρ at the beginning of the simulation due to the initial heat impulse, after which the oscillations dampen with time.

Jakobsen observed similar pressure oscillations (ringing) for the DPD fluid using a Hoover barostat (3). Figure 2 shows an expansion of the system (ρ decreases with t) to compensate for the inputted heat. Early-time behavior is displayed in the insets of figures 2a and 2b, where a sharp decrease in T_{kin} , due to the interfacial relaxation of the cold and hot regions, and the oscillating response of P_{vir} and ρ for the Hoover barostat are shown in detail. The equimolar binary DPD fluid exhibits analogous behavior, where the values of $\langle T_{kin} \rangle$, $\langle T_{int} \rangle$, $\langle P_{vir} \rangle$, and $\langle \rho \rangle$ determined at equilibrium conditions are summarized in table 4. Here again $\langle T_{kin} \rangle = \langle T_{int} \rangle$ is found, along with equivalent values of $\langle P_{vir} \rangle$ and $\langle \rho \rangle$ for the Langevin and Hoover barostats.

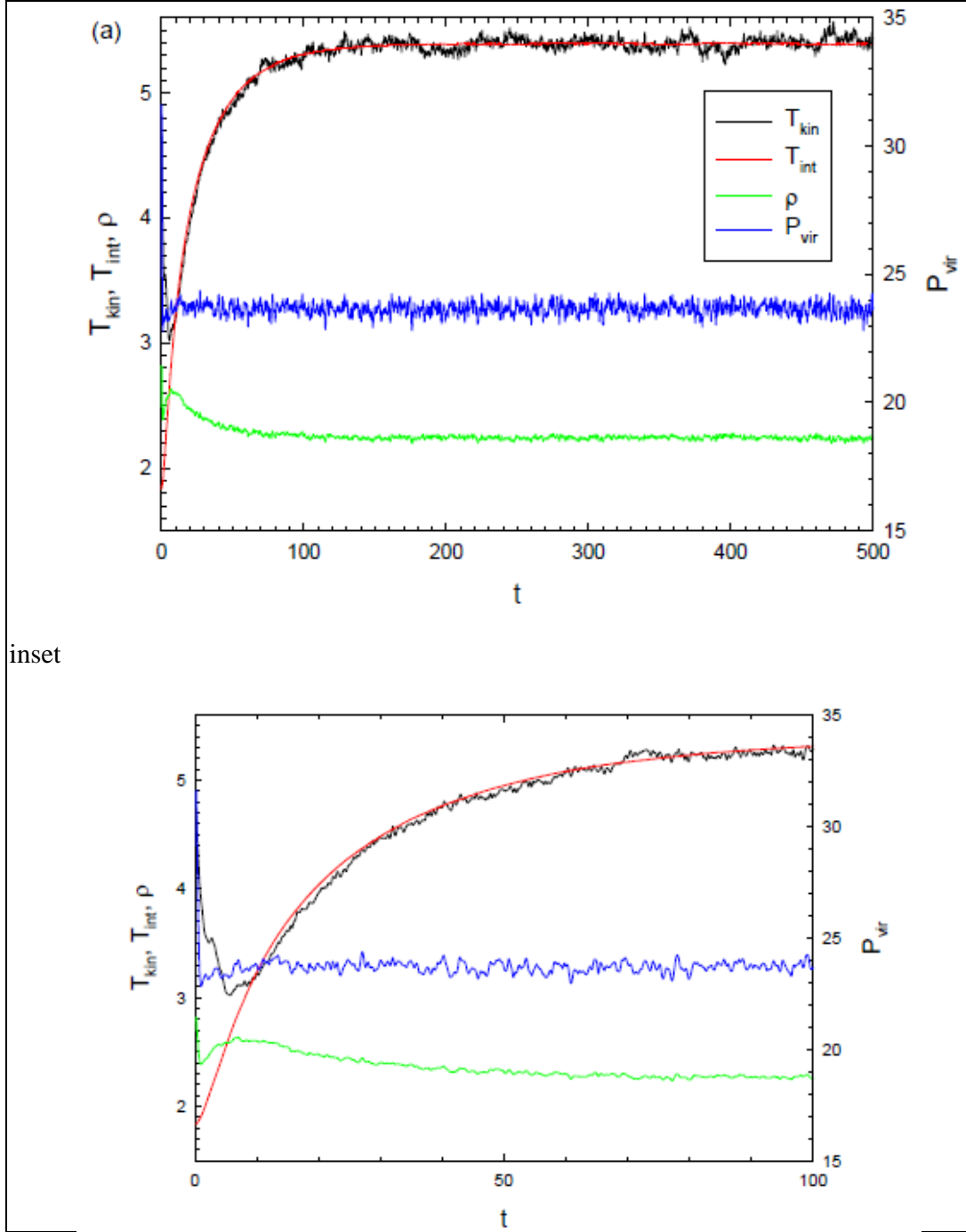


Figure 2. Time evolution of the kinetic temperature T_{kin} , internal temperature T_{int} , virial pressure P_{vir} , and particle density ρ for a DPD-H simulation of the pure DPD fluid at $P_0 = 23.65$, where a slab of particles in the simulation box was instantaneously heated by $T_{heat} = 10$ at $t = 0$: (a) DPD-H simulations using the Langevin barostat with a barostat temperature $T_{bar} = 1.0$, and (b) DPD-H simulations with a Hoover barostat. Insets display early time behavior of T_{kin} , T_{int} , ρ , and P_{vir} .

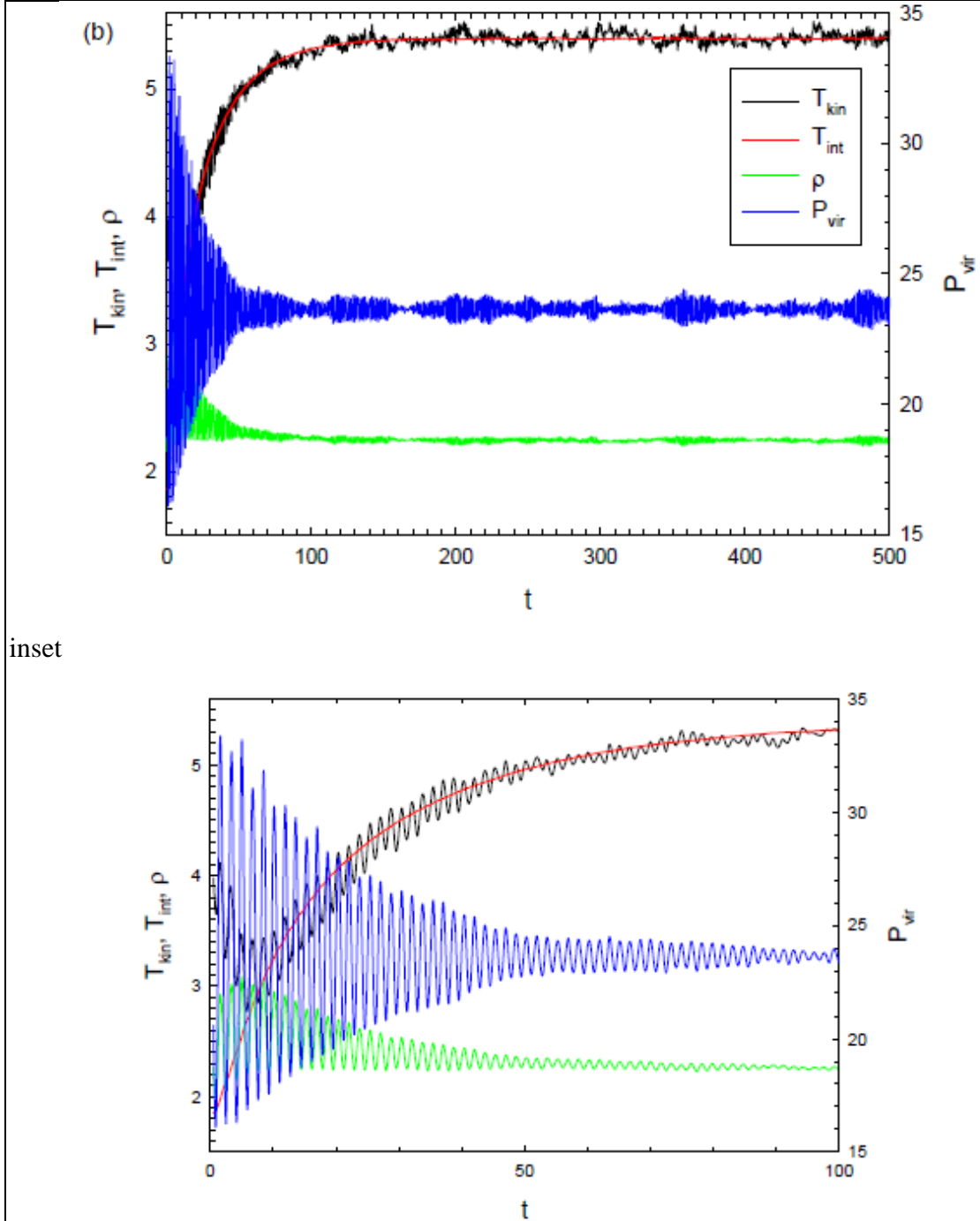


Figure 2. Time evolution of the kinetic temperature T_{kin} , internal temperature T_{int} , virial pressure P_{vir} , and particle density ρ for a DPD-H simulation of the pure DPD fluid at $P_0 = 23.65$, where a slab of particles in the simulation box was instantaneously heated by $T_{heat} = 10$ at $t = 0$: (a) DPD-H simulations using the Langevin barostat with a barostat temperature $T_{bar} = 1.0$, and (b) DPD-H simulations with a Hoover barostat. Insets display early time behavior of T_{kin} , T_{int} , ρ , and P_{vir} .

Table 4. The kinetic temperature $\langle T_{kin} \rangle$, the internal temperature $\langle T_{int} \rangle$, the virial pressure $\langle P_{vir} \rangle$, and the particle density $\langle \rho \rangle$, determined for Test Case #2 simulations of the pure and equimolar binary DPD fluids. T_{bar} is the Langevin barostat temperature and $\langle \cdot \rangle$ denotes an ensemble average, where numbers in parentheses are uncertainties calculated from block averages.

Pure DPD Fluid

Variant	$\langle T_{kin} \rangle$	$\langle T_{int} \rangle$	$\langle P_{vir} \rangle$	$\langle \rho \rangle$
DPD-E $\rho = 3$ $T_{heat} = 10$	5.405(43)	5.403(20)	37.36(14)	—
DPD-H Langevin $T_{bar} = 1.0$ $P_0 = 23.65$ $T_{heat} = 10$	5.374(41)	5.372(20)	23.65(11)	2.247(8)
DPD-H Hoover $P_0 = 23.65$ $T_{heat} = 10$	5.400(44)	5.401(20)	23.65(23)	2.243(13)

Table 4. The kinetic temperature $\langle T_{kin} \rangle$, the internal temperature $\langle T_{int} \rangle$, the virial pressure $\langle P_{vir} \rangle$, and the particle density $\langle \rho \rangle$, determined for Test Case #2 simulations of the pure and equimolar binary DPD fluids. T_{bar} is the Langevin barostat temperature and $\langle \cdot \rangle$ denotes an ensemble average, where numbers in parentheses are uncertainties calculated from block averages (continued).

Binary DPD Fluid

Variant	$\langle T_{kin} \rangle$	$\langle T_{int} \rangle$	$\langle P_{vir} \rangle$	$\langle \rho \rangle$
DPD-E $\rho = 3$ $T_{heat} = 10$	5.340(44)	5.350(16)	38.36(14)	—
DPD-H Langevin $T_{bar} = 1.0$ $P_0 = 24.79$ $T_{heat} = 10$	5.498(42)	5.507(23)	24.79(11)	2.259(8)
DPD-H Hoover $P_0 = 24.79$ $T_{heat} = 10$	5.501(43)	5.509(24)	24.79(25)	2.258(13)

4.2.2 Coarse-Grain Solid

A validation study analogous to the DPD fluid study is carried out for the coarse-grain solid model of nickel. The final configuration from the constant-temperature DPD simulation (at $T = 1300$ K and $\rho = 8260$ kg/m³) was used as the starting configuration. From this starting configuration, a slab of particles of width $0.5L$ in the middle of the simulation box was heated by assigning velocities from a Maxwell-Boltzmann distribution corresponding to T_{heat} , and by setting $u_i = C_v T_{heat}$. The remaining (nonheated) particles were assigned $u_i = C_v T_{ini}$, where $T_{ini} = T = 1300$ K. As tests of the DPD-H variants, simulations were performed at $P_0 = 0$ bar, using $T_{heat} = 3000$ K for $t_{run} = 1$ ns and $\Delta t = 5$ fs. For the DPD-H simulation, the non-uniform dilation approach with both Langevin and Hoover barostats was used; $T_{bar} = T_{ini}$ was chosen for the Langevin barostat. Relative drifts of $1.8 \cdot 10^{-4}$ in H' were observed. At low and moderate pressures, the coarse-grain solid model melts between 1800 and 1850 K (11). As a result, at the end of the DPD-H runs, the particle configuration corresponds to a liquid state. Figure 3 displays

the time evolution of T_{kin} , T_{int} , and ρ for the DPD-H simulation with the Langevin barostat. Complete melting is evidenced by reaching a plateau in the time evolution of ρ for the DPD-H simulation, where complete melting occurs at approximately 0.15 ns. Melting at constant- (V, E) conditions occurs at a slightly higher temperature (8) due to the pressure build-up within the simulation cell, which is relieved under constant (P, H) conditions. The values of $\langle T_{kin} \rangle$, $\langle T_{int} \rangle$, $\langle P_{vir} \rangle$, and $\langle \rho \rangle$ determined at equilibrium conditions are summarized in table 5, where again $\langle T_{kin} \rangle = \langle T_{int} \rangle$ is found.

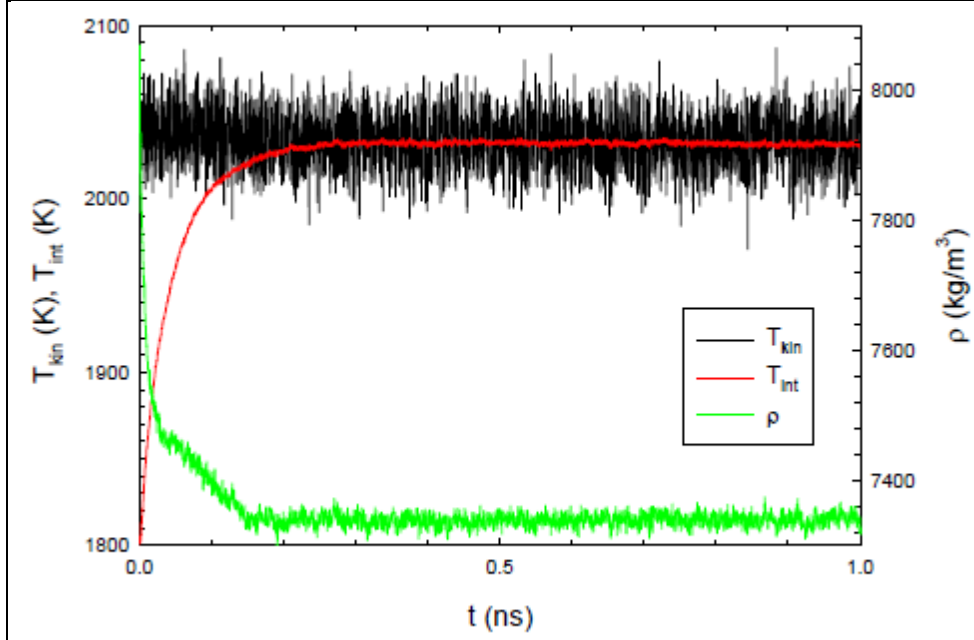


Figure 3. Time evolution of the kinetic temperature T_{kin} , internal temperature T_{int} , and mass density ρ for a DPD-H simulation using a Langevin barostat with a barostat temperature $T_{bar} = 1300$ K for the coarse-grain solid at $P_0 = 0$ bar, where a slab of particles in the simulation box was instantaneously heated by $T_{heat} = 3000$ K at $t = 0$.

Table 5. The kinetic temperature $\langle T_{kin} \rangle$, the internal temperature $\langle T_{int} \rangle$, the virial pressure $\langle P_{vir} \rangle$, and the mass density $\langle \rho \rangle$, determined for Test Case #2 simulations of the coarse-grain solid model of nickel. T_{bar} is the Langevin barostat temperature and $\langle \cdot \rangle$ denotes an ensemble average, where numbers in parentheses are uncertainties calculated from block averages.

Variant	$\langle T_{kin} \rangle$ (K)	$\langle T_{int} \rangle$ (K)	$\langle P_{vir} \rangle$ (bar)	$\langle \rho \rangle$ (kg/m ³)
DPD-E $\rho = 8260 \text{ kg/m}^3$ $T_{heat} = 3000 \text{ K}$	2060.1(146)	2060.0(28)	8863.2(55)	—
DPD-H Langevin $T_{bar} = 1300 \text{ K}$ $P_0 = 0 \text{ bar}$ $T_{heat} = 3000 \text{ K}$	2032.7(144)	2032.1(9)	0.0 (83)	7339.3(89)
DPD-H Hoover $P_0 = 0 \text{ bar}$ $T_{heat} = 3000 \text{ K}$	2034.1(143)	2033.8(8)	0.3(76)	7339.0(101)

4.3 Conservation of Total System Enthalpy

For values of Δt comparable to those used in constant-temperature DPD and DPD-P simulations, we observed a small long-term drift in H' for the DPD-H simulations. For example, for the values of Δt used for the DPD-H simulations in this work ($\Delta t = 0.01$ for the DPD fluids and $\Delta t = 5$ fs for the coarse-grain solid), the small relative drift produced in H' was typically of order 10^{-4} . When Δt was decreased by an order of magnitude, the relative drift in H' dropped to order 10^{-7} . A typical example of the dependence of the relative drift in H' on Δt for the DPD fluid is shown in figure 4. The values of other properties (not shown here), such as the kinetic and internal temperatures, configurational energy, density and virial pressure, change with Δt by less than 0.5%. This behavior is comparable with microcanonical or isoenthalpic MD simulations when the velocity-Verlet algorithm is used for the integration of the EOM (15). Since the integration of the fluctuation-dissipation contribution exactly conserves the energy (up to machine precision), the drift is caused by the velocity-Verlet algorithm during the integration of the deterministic contribution in the DPD-E or DPD-H EOM. Similar to microcanonical or isoenthalpic MD, a long-term drift in E and H' is thus inevitable in the SSA for DPD-E and DPD-H.

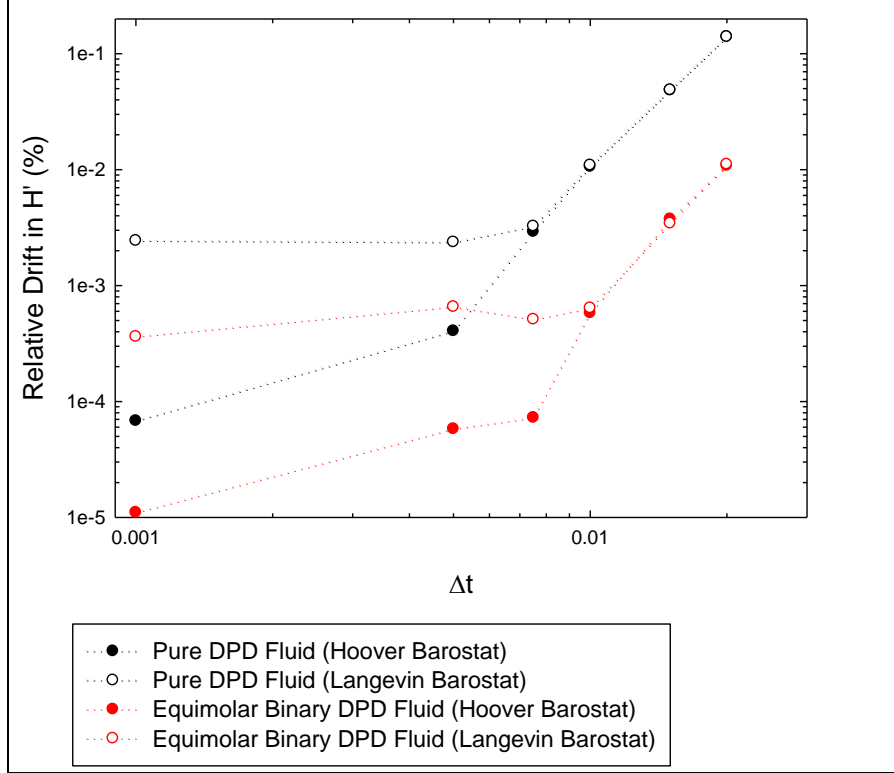


Figure 4. The relative drift in H' as a function of the integration time step Δt for DPD-H simulations with the SSA-VV.

To enforce enthalpy beyond this small drift, one can apply the following numerical procedure. After each time step, the difference between the current H' and the inputted H' is calculated. This difference is then divided by the number of particles and equally subtracted from each u_i . This is a useful strategy provided that the drift in H' has a mechanical origin, which implies that the energy drift scales as $k_B T$. Thus, the extra energy per particle subtracted in this procedure is very small compared to the magnitude of u_i , which scales as $C_v T$. In this work, the variation of the system temperature due to this drift was found to be negligible and the dynamics unaffected. This strategy was applied to all test cases for DPD-H with a Hoover barostat, where no variation in the results was observed. Note that H' is not a fixed quantity for DPD-H with a Langevin barostat (rather it fluctuates about an average of H'); therefore, this error suppression scheme can only be applied to DPD-H with a Hoover barostat.

5. Conclusion

An isoenthalpic, isobaric DPD method was developed by combining the equations of motion from both the DPD-P and DPD-E methods. Both Hoover and Langevin barostats were implemented, where an additional barostat parameter, the barostat temperature, was defined for the DPD-H variant with the Langevin barostat. A comprehensive description of a numerical integration scheme based upon the Shardlow-splitting algorithm was presented for the DPD-H approach, which was found to be a readily extendable and accurate integration scheme.

The equivalence of the DPD-H variant was verified using both a standard DPD fluid model and a coarse-grain solid model, where thermodynamic quantities as well as probability distributions were considered. The integration algorithm was further verified by considering equilibrium and nonequilibrium simulation scenarios. Finally, a discussion of the inevitable small, long-term drift in H' associated with finite integration methods was given, where we propose a simple strategy to minimize the effect of this drift in DPD-H simulations.

6. References

1. Bonet Avalos, J.; Mackie, A. D. Dissipative Particle Dynamics With Energy Conservation. *Europhys. Lett.* **1997**, *40* (2), 141.
2. Español, P. Dissipative Particle Dynamics With Energy Conservation. *Europhys. Lett.* **1997**, *40* (6), 631.
3. Jakobsen, A. F. Constant-Pressure and Constant-Surface Tension Simulations in Dissipative Particle Dynamics. *J. Chem. Phys.* **2005**, *122*, 124901.
4. Trofimov, S. Y.; Nies E. L. F.; Michels, M. A. J. Constant-Pressure Simulations With Dissipative Particle Dynamics. *J. Chem. Phys.* **2005**, *123*, 144102.
5. Weingarten, N. S.; Mattson, W. D.; Yau, A. D.; Weihs, T. P.; Rice, B. M. A Molecular Dynamics Study of the Role of Pressure on the Response of Reactive Materials to Thermal Initiation. *J. Appl. Phys.* **2010**, *107*, 093517.
6. Brennan, J. K.; Lísal, M. *Dissipative Particle Dynamics at Isothermal Conditions Using Shardlow-Like Splitting Algorithms*; ARL-TR-6582; U.S. Army Research Laboratory: Aberdeen Proving Ground, MD, September 2013.
7. Brennan, J. K.; Lísal, M. *Dissipative Particle Dynamics at Isothermal, Isobaric Conditions Using Shardlow-Like Splitting Algorithms*; ARL-TR-6583; U.S. Army Research Laboratory: Aberdeen Proving Ground, MD, September 2013.
8. Brennan, J. K.; Lísal, M. *Dissipative Particle Dynamics at Isoenergetic Conditions Using Shardlow-Like Splitting Algorithms*; ARL-TR-6586; U.S. Army Research Laboratory: Aberdeen Proving Ground, MD, September, 2013.
9. Shardlow, T. Splitting for Dissipative Particle Dynamics. *SIAM J. Sci. Comput.* **2003**, *24*, 1267.
10. Groot, R. D.; Warren, P. B. Dissipative Particle Dynamics: Bridging the Gap Between Atomistic and Mesoscopic Simulation. *J. Chem. Phys.* **1997**, *107*, 4423.
11. Brennan, J. K.; Lísal, M. *Proceedings of the 14th International Detonation Symposium*, Coeur d'Alene, ID, 11–16 April 2010; Office of Naval Research, 2010, p 1451.
12. Pagonabarraga, I.; Frenkel, D. Dissipative Particle Dynamics for Interacting Systems. *J. Chem. Phys.* **2001**, *115*, 5015.
13. Merabia, S.; Bonet Avalos, J. Dewetting of a Stratified Two-Component Liquid Film on a Solid Substrate. *J. Phys. Rev. Lett.* **2008**, *101*, 208303.

14. Callen, H. B. *Thermodynamics and an Introduction to Thermostatistics*; Wiley: New York, 1985.
15. Allen, M. P.; Tildesley, D. J. *Computer Simulation of Liquids*; Clarendon Press: Oxford, UK, 1987.
16. Martyna, G. J.; Tuckerman, M. E.; Tobias, D. J.; Klein, M. L. Explicit Reversible Integration Algorithms for Extended Systems. *Mol. Phys.* **1996**, *87*, 1117.
17. McQuarrie, D. A. *Statistical Mechanics*; University Science Books: Mill Valley, CA, 2000.
18. Ripoll, M.; Español, P.; Ernst, M. H. Dissipative Particle Dynamics with Energy Conservation: Heat Conduction. *Int. J. Mod. Phys. C* **1998**, *9* (8), 1329–1338.
19. Mackie, A. D.; Bonet Avalos, J.; Navas, V. Dissipative Particle Dynamics With Energy Conservation: Modelling of Heat Flow. *Phys. Chem. Chem. Phys.* **1999**, *1*, 2039.
20. Quigley, D.; Probert, M. I. J. Langevin Dynamics in Constant Pressure Extended Systems. *J. Chem. Phys.* **2004**, *120*, 11432.

INTENTIONALLY LEFT BLANK.

**Appendix A. Fokker-Planck Equation (FPE) and Fluctuation-Dissipation
Theorem (FDT)**

The FPE corresponding to the equation of motion (EOM) given by equation 5 of the technical report is

$$\frac{\partial \rho}{\partial t} = L_C \rho + L_D \rho + L_{cond} \rho + L_{LB} \rho, \quad (\text{A-1})$$

where $\rho \equiv \rho(\mathbf{r}, \mathbf{p}, V, p_\varepsilon, u; t)$. The conservative operator L_C is given by

$$L_C \equiv - \left(\sum_i \frac{\mathbf{p}_i}{m_i} \cdot \frac{\partial}{\partial \mathbf{r}_i} + \sum_i \sum_{j \neq i} \mathbf{F}_{ij}^C \cdot \frac{\partial}{\partial \mathbf{p}_i} \right) - \left[\frac{p_\varepsilon}{W_\varepsilon} \sum_i \mathbf{r}_i \cdot \frac{\partial}{\partial \mathbf{r}_i} - \left(1 + \frac{d}{N_f} \right) \frac{p_\varepsilon}{W_\varepsilon} \sum_i \mathbf{p}_i \cdot \frac{\partial}{\partial \mathbf{p}_i} \right] - \frac{dV}{dt} \frac{\partial}{\partial V} - \left[dV(P - P_0) + \frac{d}{N_f} \sum_i \frac{\mathbf{p}_i \cdot \mathbf{p}_i}{m_i} \right] \frac{\partial}{\partial p_\varepsilon}. \quad (\text{A-2})$$

The operator L_D representing the effects of the dissipative and random forces is given by

$$L_D \equiv \sum_i \sum_{j \neq i} \frac{\mathbf{r}_{ij}}{r_{ij}} \cdot \left(\frac{\partial}{\partial \mathbf{p}_i} - \frac{\mathbf{v}_{ij}}{2} \frac{\partial}{\partial u_i} \right) \left[\gamma_{ij} \omega^D \left(\frac{\mathbf{r}_{ij}}{r_{ij}} \cdot \mathbf{v}_{ij} \right) + \frac{\sigma_{ij}^2}{2} (\omega^R)^2 L_{ij} \right] \\ L_{ij} = \frac{\mathbf{r}_{ij}}{r_{ij}} \cdot \left[\frac{\partial}{\partial \mathbf{p}_i} - \frac{\partial}{\partial \mathbf{p}_j} - \frac{\mathbf{v}_{ij}}{2} \left(\frac{\partial}{\partial u_i} + \frac{\partial}{\partial u_j} \right) \right]. \quad (\text{A-3})$$

The operator L_{cond} associated with the effects of the mesoscopic heat transfer between particles is given by

$$L_{cond} \equiv - \left\{ \sum_i \sum_{j \neq i} \omega^{Dq} \frac{\partial}{\partial u_i} \left[\kappa_{ij} \left(\frac{1}{\theta_i} - \frac{1}{\theta_j} \right) \right] - \frac{1}{2} (\omega^{Rq})^2 \frac{\partial}{\partial u_i} \left[\alpha_{ij}^2 \left(\frac{\partial}{\partial u_i} - \frac{\partial}{\partial u_j} \right) \right] \right\}, \quad (\text{A-4})$$

with the condition $\left(\frac{\partial}{\partial u_i} - \frac{\partial}{\partial u_j} \right) \alpha_{ij}^2 = 0$ to ensure that the EOM contain no spurious drift.

The operator L_{LB} representing the Langevin barostat terms in the EOM is given by

$$L_{LB} \equiv \frac{\partial}{\partial p_\varepsilon} \left(\gamma_P p_\varepsilon + \frac{\sigma_P^2}{2} \frac{\partial}{\partial p_\varepsilon} \right). \quad (\text{A-5})$$

Analogous to the constant-energy (DPD-E) variant, an implicit heat reservoir is not present in constant-enthalpy Dissipative Particle Dynamics (DPD-H), nor is the total system enthalpy specified in the FPE (A-1). Therefore, to simplify the derivation of the FDT for DPD-H, we

choose the isothermal-isobaric ensemble. Under the steady-state condition, $\rho^{eq} \equiv \rho^{eq}(\mathbf{r}, \mathbf{p}, V, p_\varepsilon, u)$ corresponds to the probability density.^{1,2,3}

$$\rho^{eq}(\mathbf{r}, \mathbf{p}, V, p_\varepsilon, u) = \frac{1}{\Omega} \exp \left[- \frac{\sum_i \frac{\mathbf{p}_i \cdot \mathbf{p}_i}{2m_i} + \sum_i \sum_{j>i} u_{ij}^{CG} + P_0 V + \frac{p_\varepsilon^2}{2W_\varepsilon}}{k_B T} \right] \prod_i \exp \left[\frac{s_i(u_i)}{k_B} - \frac{u_i}{k_B T} \right]. \quad (\text{A-6})$$

Analogous to the previous cases 6–8, $L_C \rho^{eq} = 0$ for the equilibrium distribution. The FDT then follows from the requirements that $L_D \rho^{eq} = 0$, $L_{cond} \rho^{eq} = 0$ and $L_{LB} \rho^{eq} = 0$, which lead to equations (6) and (7) given in the report. As mentioned in the report, while the FDT relations relevant to the dynamics of the particles depend only on particle variables, the FDT relevant to the Langevin barostat depends on the heat reservoir temperature. For constant-pressure DPD, this temperature is simply the system temperature; however, in constant-enthalpy DPD, the heat reservoir temperature (i.e., barostat temperature) becomes an additional Langevin barostat parameter along with γ_p , σ_p , and W_ε , which can be written as

$$\sigma_p^2 = 2\gamma_p W_\varepsilon k_B T_{bar}, \quad (\text{A-7})$$

where T_{bar} is the Langevin barostat temperature. Interestingly, a Hoover barostat is a purely mechanical barostat with no dissipation (nor an associated barostat temperature); hence, the volume fluctuations are only a result of the inherent thermal perturbations from the motions of the particles. In contrast, a Langevin barostat incorporates dissipation via the friction and random terms in F_ε (see equation 5 of the report); thus the volume fluctuations of the system will additionally depend on the value of T_{bar} . (As an illustrative analogy, one can consider the Hoover barostat as a piston in a vacuum, while the Langevin barostat can be viewed as a piston in a viscous fluid, whose temperature-dependent viscosity affects the piston fluctuations.)

To demonstrate the effects of T_{bar} on the system properties, we carried out DPD-H simulations using the Langevin barostat with $T_{bar} = \{0.5, 1.0, 1.5, 2.0\}$ for the DPD fluid. We also performed DPD-H simulations using the Hoover barostat, where all simulation results are summarized in table A-1. The table clearly shows that the values of the volume fluctuation δV^2 and the associated isentropic compressibility depend on T_{bar} , while thermodynamic properties such as the configurational energy per particle, kinetic temperature, internal temperature, virial pressure, and particle density are, as expected, not affected by T_{bar} . Additionally, figure A-1 displays the

¹Jakobsen, A. F. Constant-Pressure and Constant-Surface Tension Simulations in Dissipative Particle Dynamics. *J. Chem. Phys.* **2005**, *122*, 124901.

²Mackie, A. D.; Bonet Avalos, J.; Navas, V. Dissipative Particle Dynamics With Energy Conservation: Modelling of Heat Flow. *Phys. Chem. Chem. Phys.* **1999**, *1*, 2039.

³Quigley, D.; Probert, M. I. J. Langevin Dynamics in Constant Pressure Extended Systems. *J. Chem. Phys.* **2004**, *120*, 11432.

volume probability distributions for the Langevin barostat at different T_{bar} and for the Hoover barostat, which further elaborates the effects of T_{bar} on δV^2 . In table A-1 and figure A-1, the volume fluctuations corresponding to the Langevin barostat with $T_{bar} = 1.0$ and those corresponding to the Hoover barostat are nearly equivalent since $T_{bar} = 1.0$ is close to the equilibrium system temperature of approximately 0.986. If T_{bar} was set to the value of the equilibrium system temperature, the volume fluctuations given by the Langevin barostat and those given by the Hoover barostat would match precisely.

Table A-1. The configurational energy per particle $\langle u \rangle$, the kinetic temperature $\langle T_{kin} \rangle$, the internal temperature $\langle T_{int} \rangle$, the virial pressure $\langle P_{vir} \rangle$, the particle density $\langle \rho \rangle$, the isentropic compressibility κ_S , and the volume fluctuation δV^2 for the DPD fluid at various values of the Langevin barostat temperature, T_{bar} . $\langle \cdot \rangle$ denotes an ensemble average, where numbers in parentheses are uncertainties calculated from block averages. These simulations were all started from the same final configuration of a constant-temperature DPD simulation at $T = 1$ and particle density $\rho = 3$. The imposed pressure $P_0 = 23.65$ corresponds to $\langle P_{vir} \rangle$ from the constant-temperature DPD simulation. Since $C_V / k_B = 60$ was used in the coarse-grain particle equation-of-state, equilibrium temperatures should be $1 - k_B / C_V \cong 0.983$; C_V is the heat capacity.

Barostat	$\langle u \rangle$	$\langle T_{kin} \rangle$	$\langle T_{int} \rangle$	$\langle P_{vir} \rangle$	$\langle \rho \rangle$	$\kappa_S \times 10^1$	δV^2
Hoover Barostat	4.542(19)	0.986(8)	0.986(1)	23.65(14)	3.002(13)	0.207	68.76
Langevin Barostat $T_{bar} = 0.5$	4.541(14)	0.986(8)	0.985(1)	23.65(10)	3.002(10)	0.110	36.58
Langevin Barostat $T_{bar} = 1.0$	4.541(19)	0.986(8)	0.986(1)	23.65(13)	3.002(12)	0.209	69.37
Langevin Barostat $T_{bar} = 1.5$	4.542(20)	0.986(8)	0.986(1)	23.66(13)	3.003(13)	0.308	102.3
Langevin Barostat $T_{bar} = 2.0$	4.542(26)	0.986(8)	0.986(1)	23.65(9)	3.002(11)	0.417	138.59

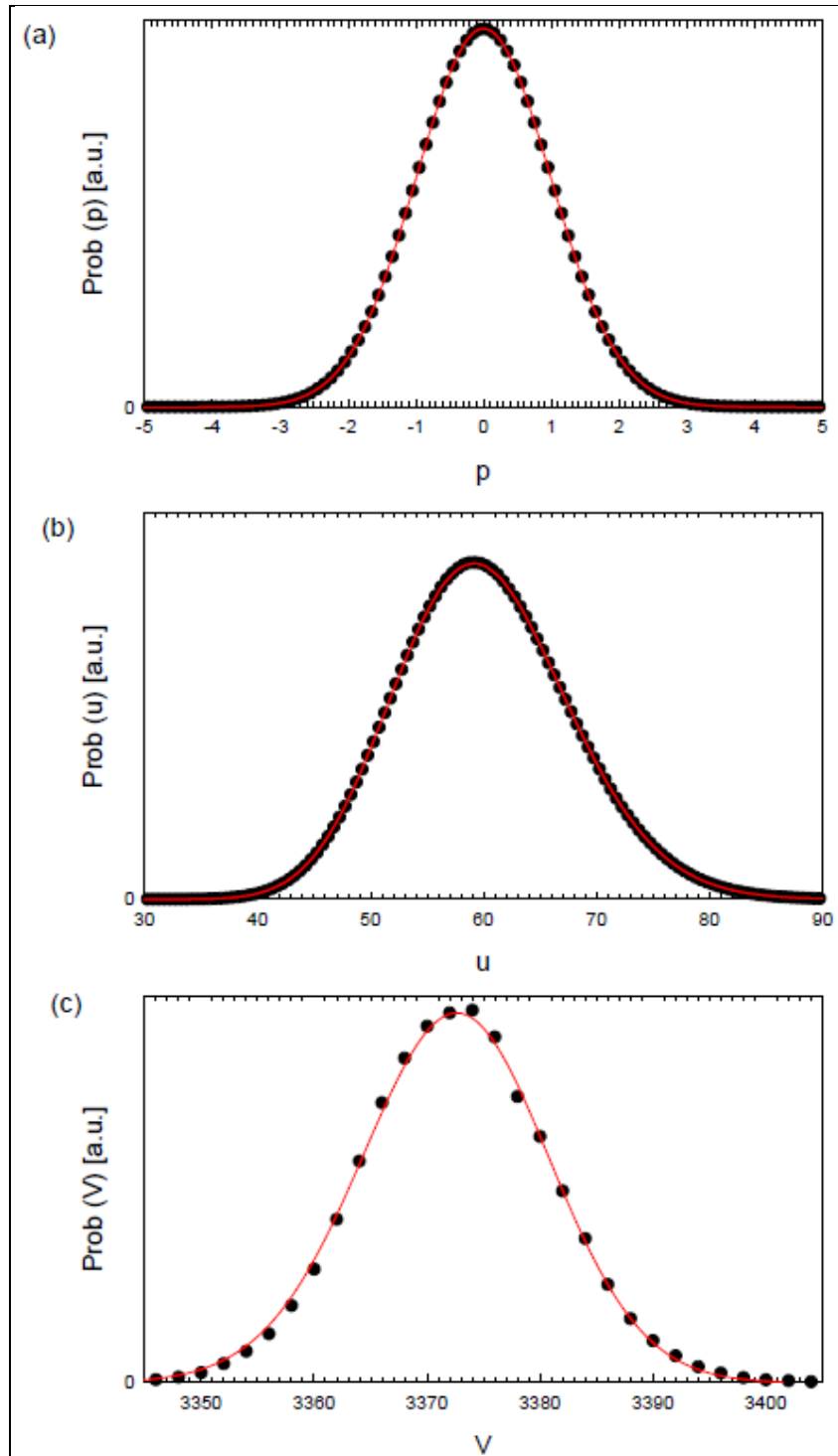


Figure A-1. The probability distributions of (a) p_i , (b) u_i , and (c) V for DPD-H with a Langevin barostat. Symbols represent simulation results for $\Delta t = 0.01$, and lines correspond to (a) the Maxwell-Boltzmann distribution for p_i and (b, c) “exact” results, i.e., simulation results where $\Delta t = 0.001$.

INTENTIONALLY LEFT BLANK.

**Appendix B. Constant-Enthalpy Conditions (DPD-H) for Nonuniform
Dilation**

Following the derivation of the uniform dilation constant-enthalpy conditions (DPD-H) variant, the combined equations of motion for non-uniform dilation using a Langevin barostat and constant-energy conditions (DPD-E) are given as

$$\begin{aligned}
dr_{i,\alpha} &= \frac{p_{i,\alpha}}{m_i} dt + \frac{p_{\varepsilon,\alpha}}{W_\varepsilon} r_{i,\alpha} dt \\
dp_{i,\alpha} &= \sum_{j \neq i} (F_{ij,\alpha}^C + F_{ij,\alpha}^D + F_{ij,\alpha}^R) dt - \frac{p_{\varepsilon,\alpha}}{W_\varepsilon} p_{i,\alpha} dt \\
&\quad - \frac{p_{\varepsilon,x} + p_{\varepsilon,y} + p_{\varepsilon,z}}{3N_f W_\varepsilon} p_{i,\alpha} dt \quad (i = 1, \dots, N) \\
d \ln L_\alpha &= \frac{p_{\varepsilon,\alpha}}{W_\varepsilon} dt \\
dp_{\varepsilon,\alpha} &= F_{\varepsilon,\alpha} dt \\
du_i^{mech} &= \frac{1}{2} \sum_{j \neq i} \gamma_{ij} \omega^D \left(\frac{\mathbf{r}_{ij}}{r_{ij}} \cdot \mathbf{v}_{ij} \right)^2 dt - \frac{d\sigma_{ij}^2}{2} \left(\frac{1}{m_i} + \frac{1}{m_j} \right) (\omega^R)^2 dt \quad (i = 1, \dots, N) \\
&\quad - \sigma_{ij} \omega^R \left(\frac{\mathbf{r}_{ij}}{r_{ij}} \cdot \mathbf{v}_{ij} \right) dW_{ij} \\
du_i^{cond} &= \sum_{j \neq i} \kappa_{ij} \left(\frac{1}{\theta_i} - \frac{1}{\theta_j} \right) \omega^{Dq} dt + \alpha_{ij} \omega^{Rq} dW_{ij}^q
\end{aligned} \tag{B-1}$$

where d is the dimensionality of the system and the variables ε_α , $p_{\varepsilon,\alpha}$, W_ε , V , $F_{\varepsilon,\alpha}$, and $P_{\alpha\beta}$ are the same as in the non-uniform dilation DPD-P variant, except $\sigma_p^2 = 2\gamma_p W_\varepsilon k_B T_{bar}$, and T_{bar} is the Langevin barostat temperature. Variables pertaining to u_i^{mech} and u_i^{cond} are the same as those in the uniform dilation DPD-H variant.

B.1 Numerical Discretization

Applying a numerical integration splitting strategy similar to the uniform dilation DPD-H variant, the deterministic differential equations and the elementary constant-energy (SDEs) corresponding to equation (B-1) are the following. The conservative terms are the same as those for the non-uniform dilation constant pressure conditions (DPD-P) variant,¹ while the fluctuation-dissipation terms are identical to the expressions given in equation 11 of the report.

¹Bonet Avalos, J.; Mackie, A. D. Dissipative Particle Dynamics With Energy Conservation. *Europhys. Lett.* **1997**, *40* (2), 141.

As stated in the report, the stochastic flow map $\phi_{\Delta t}$ is approximated by equation 12 of the report. For each fluctuation-dissipation term $\phi_{\Delta t;i,j}^{diss}$, momenta and internal energies are updated by using the same expressions as in the uniform dilation DPD-H variant for the constant energy (SSA-VV) scheme (equations 13a and 13b of the report). $\phi_{\Delta t}^C$ can be treated in identical fashion to the nonuniform dilation DPD-P variant.

INTENTIONALLY LEFT BLANK.

Appendix C. Simulation Model Details

For the models considered in this work, the details of the conservative forces expressed in equation 2 of the main text are the following. u_{ij}^{CG} for the pure and binary constant-temperature Dissipative Particle Dynamics (DPD) fluids is given by

$$u_{ij}^{CG} = a_{ij} r_c \omega^D(r_{ij}), \quad (\text{C-1})$$

where a_{ij} is the maximum repulsion between particle i and particle j .

For the coarse-grain solid model, which has a face-centered-cubic (f.c.c.) lattice structure, particles interact through a shifted-force Sutton-Chen embedded potential (SC) given as:

$$u_i^{CG} = \varepsilon \left(\frac{1}{2} \sum_{j \neq i} u_{ij}^{rep} - c \sqrt{\rho_i} \right), \quad (\text{C-2})$$

where

$$\begin{aligned} u_{ij}^{rep} &= v(r_{ij}) - v(r_{ij} = r_c) - \left. \frac{dv(r_{ij})}{dr_{ij}} \right|_{r_{ij}=r_c} (r_{ij} - r_c) \\ v(r_{ij}) &= \left(\frac{r_0}{r_{ij}} \right)^n \\ \rho_i &= \sum_{j \neq i} \rho_{ij} \\ \rho_{ij} &= w(r_{ij}) - w(r_{ij} = r_c) - \left. \frac{dw(r_{ij})}{dr_{ij}} \right|_{r_{ij}=r_c} (r_{ij} - r_c) \\ w(r_{ij}) &= \left(\frac{r_0}{r_{ij}} \right)^m \end{aligned} \quad (\text{C-3})$$

ε and r_0 are the energy and length parameters, respectively, n and m are positive integers ($n > m$ to satisfy elastic stability of the crystal), and c is a dimensionless parameter. Although effectively this is a many-body potential, the force on each particle can be written as a sum of pair-wise contributions. The coarse-grain solid model used here approximates nickel (Ni), where one constant-temperature Dissipative Particle Dynamics (DPD) particle was chosen to represent four f.c.c. unit cells, i.e., 16 Ni atoms. SC potential parameters were determined by fitting to various 0-K properties and the melting temperature at zero pressure,¹ where the following values were found: $\varepsilon/k_B = 225$ K, $r_0 = 8.8698$ Å, $c = 39.4314$, $m = 6$, and $n = 9$. Further details for determining SC parameters based upon such a procedure can be found elsewhere and references therein.¹

¹Brennan, J. K.; Lísal, M. *Proceedings of the 14th International Detonation Symposium*, Coeur d'Alene, ID, 11–16 April 2010; Office of Naval Research, 2010, p 1451.

List of Symbols, Abbreviations, and Acronyms

DPD	constant-temperature Dissipative Particle Dynamics
DPD-E	constant-energy Dissipative Particle Dynamics
DPD-H	constant-enthalpy Dissipative Particle Dynamics
EOM	equations of motion
f.c.c.	face-centered-cubic
FDT	fluctuation-dissipation theorem
FPE	Fokker-Planck equation
MD	molecular dynamics
SC	Sutton-Chen embedded potential
SSA	Shardlow-splitting algorithm

NO. OF
COPIES ORGANIZATION

1 DEFENSE TECHNICAL
(PDF) INFORMATION CTR
DTIC OCA

1 DIRECTOR
(PDF) US ARMY RESEARCH LAB
IMAL HRA

1 DIRECTOR
(PDF) US ARMY RESEARCH LAB
RDRL CIO LL

1 GOVT PRINTG OFC
(PDF) A MALHOTRA

ABERDEEN PROVING GROUND

1 DIR USARL
(PDF) RDRL WML B
J BRENNAN